

A Long Baseline Neutrino Oscillation Experiment

Using J-PARC Neutrino Beam

and Hyper-Kamiokande

(Dated: April 14, 2014)

Abstract

Hyper-Kamiokande will be a next generation underground water Cherenkov detector with a total (fiducial) mass of 0.99 (0.56) million metric tons, approximately 20 (25) times larger than that of Super-Kamiokande. It is designed as a detector capable of observing accelerator, atmospheric and solar neutrinos, proton decays, and neutrinos from other astrophysical origins, providing rich scientific programs. One of the main goals of Hyper-Kamiokande is the study of CP asymmetry in the lepton sector using accelerator neutrino and anti-neutrino beams.

In this document, the physics potential of a long baseline neutrino experiment using the Hyper-Kamiokande detector and a neutrino beam from the J-PARC proton synchrotron is presented. The analysis has been updated from the previous Letter of Intent [K. Abe et al., arXiv:1109.3262 [hep-ex]], based on the experience gained from the ongoing T2K experiment. With a total exposure of $7.5 \text{ MW} \times 10^7 \text{ sec}$ integrated proton beam power (corresponding to 1.56×10^{22} protons on target with a 30 GeV proton beam) to a 2.5-degree off-axis neutrino beam produced by the J-PARC proton synchrotron, it is expected that the CP phase δ_{CP} can be determined to better than 19 degrees for all possible values of δ_{CP} , and CP violation can be established with a statistical significance of more than 3σ (5σ) for 76% (58%) of the δ_{CP} parameter space.

The Hyper-Kamiokande Working Group

Boston University (USA): E. Kearns, J.L. Stone

Chonnam National University (Korea): K.K. Joo, J.Y. Kim, I.T. Lim

Dongshin University (Korea): M.Y. Pac, J.H. Choi

Duke University (USA): A. Himmel, K. Scholberg, C.W. Walter

Earthquake Research Institute, The University of Tokyo (Japan): A. Taketa, H.K.M. Tanaka

ETH Zurich (Switzerland): F Bay, S Di Luise, A. Rubbia

Imperial College London (UK): M. Malek, Y. Uchida, M.O. Wascko

Institute for Particle Physics Phenomenology, Durham University (UK): P. Ballett,
S. Pascoli, M. Ross-Lonergan

INFN and Dipartimento Interateneo di Fisica di Bari (Italy): V. Berardi, M.G. Catanesi,
R.A. Intonti, L. Magaletti, E. Radicioni

INFN-LNF (Italy): A. Longhin

INFN and Università di Napoli (Italy): G. De Rosa, V. Palladino, C. Riccio

INFN and Università di Padova (Italy): G. Collazuol, M. Laveder, M. Mezzetto

INFN Roma (Italy): L. Ludivici

Institute for Nuclear Research (Russia): A. Izmaylov, M. Khabibullin, A. Khotjantsev,
Y. Kudenko, O. Mineev, A. Shaikhiev, N. Yershov

Iowa State University (USA): I. Anghel, G. Davies, M.C. Sanchez, T. Xin

IRFU, CEA Saclay (France): S. Bolognesi, S. Emery, V. Galymov, E. Mazzucato, G. Vasseur,
M. Zito

Kamioka Observatory, ICRR, The University of Tokyo (Japan): K. Abe, Y. Haga,
Y. Hayato, M. Ikeda, J. Kameda, Y. Kishimoto, M. Miura, S. Moriyama, M. Nakahata, S. Nakayama,
H. Sekiya, M. Shiozawa, A. Takeda, H. Tanaka, T. Tomura, R. Wendell

Kavli IPMU (WPI), The University of Tokyo (Japan): M. Hartz, L. Marti, K. Nakamura,
Y. Suzuki, M.R. Vagins

KEK (Japan): M. Friend, Y. Fujii, T. Ishida, T. Kobayashi, Y. Oyama, T. Sekiguchi

Kobe University (Japan): A. T. Suzuki, Y. Takeuchi, T. Yano

Kyoto University (Japan): C. Bronner, S. Hirota, K. Huang, A.K. Ichikawa, M. Jiang, A. Minamino, T. Nakaya

Laboratoire Leprince-Ringuet, Ecole Polytechnique (France): O. Drapier, M. Gonin, T. Mueller, B. Quilain

Lancaster University (UK): A. Finch, L.L. Kormos, J. Nowak, H.M. O’Keeffe, P.N. Ratoff

Los Alamos National Laboratory (USA): G. Sinnis

Louisiana State University (USA): F.d.M. Blaszczyk, J. Insler, T. Kutter, O. Perevozchikov, M. Tzanov

Miyagi University of Education (Japan): Y. Fukuda

Nagoya University (Japan): K. Choi, T. Iijima, Y. Itow

National Centre for Nuclear Research (Poland): J. Lagoda, E. Rondio

Okayama University (Japan): D. Fukuda, H. Ishino, Y. Koshio, T. Mori, M. Sakuda

Osaka City University (Japan): Y. Seiya, K. Yamamoto

Pontificia Universidade Católica do Rio de Janeiro (Brazil): H. Nunokawa

Queen Mary, University of London (UK): L. Cremonesi, F. Di Lodovico, T. Katori, P.P.J. Martins, R.A. Owen, R. Sacco, S. Short, R. Terri, J.R. Wilson

Research Center for Cosmic Neutrinos, ICRR, The University of Tokyo (Japan): T. Irvine, T. Kajita, Y. Nishimura, K. Okumura, E. Richard

Royal Holloway University of London (UK): T. Berry, J. Monroe

Seoul National University (Korea): S.B. Kim

Seoyeong University (Korea): H.I. Jang

State University of New York at Stony Brook (USA): J. Imber, C.K. Jung, C. McGrew, J.L. Palomino, C. Yanagisawa

STFC Rutherford Appleton Laboratory (UK): C. Densham, M. Fitton, T. Nicholls, T. Stewart, M. Thorpe

Sungkyunkwan University (Korea): C. Rott

The California State University Dominguez Hills (USA): K. Ganezer, B. Hartfiel, J. Hill

Tohoku University (Japan): K. Inoue, M. Koga, I. Shimizu

Tokyo Institute of Technology (Japan): M. Ishitsuka, M. Kuze, Y. Okajima

TRIUMF (Canada): P. Gumplinger, A. Konaka, T. Lindner, K. Mahn, J.-M. Poutissou, F. Retiere, M. Scott, M.J. Wilking, S. Yen

University Autonoma Madrid (Spain): P. Fernández, L. Labarga, J. Pérez

University of Bern (Switzerland): A. Ariga, T. Ariga, A. Ereditato, M. Hierholzer, M. Nirkko, C. Pistillo, A. Redij

University of British Columbia (Canada): S. Berkman, T. Feusels, S.M. Oser, H.A. Tanaka, S. Tobayama

University of California, Davis (USA): M. Askins, M. Bergevin, R. Svoboda

University of California, Irvine (USA): G. Carminati, S. Horiuchi, W.R. Kropp, S. Mine, M.B. Smy, H.W. Sobel

University of Edinburgh (UK): P. Beltrame, G. Cowan, F. Muheim, M. Needham

University of Geneva (Switzerland): A. Blondel, A. Bravar, Y. Karadzhov, A. Korzenev, E. Noah, M. Ravonel, M. Rayner, R. Asfandiyarov, L. Haegel, A. Haesler, C. Martin, E. Scantamburlo

University of Hawaii (USA): J.G. Learned

University of Liverpool (UK): C. Andreopoulos, N. McCauley, D. Payne, H.J. Rose, C. Touramanis

University of Oxford (UK): G. Barr, D. Dewhurst, D. Wark, A. Weber

University of Pittsburgh (USA): V. Paolone

University of Regina (Canada): M. Barbi, R. Tacik

University of Rochester (USA): K.S. McFarland

Universidade de São Paulo (Brazil): H. Minakata

University of Sheffield (UK): S.L. Cartwright, J.D. Perkin, L.F. Thompson

University of Tokyo (Japan): H. Aihara, Y. Suda, M. Yokoyama

University of Toronto (Canada): J.F. Martin

University of Warsaw (Poland): M. Posiadala-Zezula

University of Warwick (UK): J.J. Back, G.J. Barker, S.B. Boyd, D.R. Hadley

University of Washington (USA): J. Detwiler, N. Tolich, R.J. Wilkes

University of Winnipeg (Canada): B. Jamieson

Virginia Tech (USA): C. Mariani, S.D. Rountree, R.B. Vogelaar

Wroclaw University (Poland): J. Sobczyk

York University (Canada): S. Bhadra

CONTENTS

I. Introduction	9
A. Introduction to Neutrino Oscillations and CP violation	10
B. Expected results from T2K, NO ν A and reactor experiments	12
C. Vision of Neutrino Physics in the 2020s	15
1. Uniqueness of Hyper-Kamiokande with the J-PARC neutrino beam	15
2. Other planned experiments: LBNE, LBNO and others	16
D. Overall Science goals of the Hyper-Kamiokande project	17
II. The Hyper-Kamiokande Detector	18
A. Site, caverns, and tanks	18
B. Water purification system	22
C. Photosensors	23
D. Electronics and data acquisition system	26
E. Detector calibration	28
F. Expected detector performance	29
III. Neutrino Beam at J-PARC	32
A. J-PARC accelerator cascade and the neutrino experimental facility	32
B. Power upgrade of Main Ring synchrotron and the neutrino beamline	34
C. The neutrino flux calculation	37
1. The flux uncertainties	37
2. The neutrino beam direction	40
IV. Near Detectors	41
A. Neutrino cross section uncertainties relevant for near detector requirements	41
B. The T2K near detectors	43
1. The T2K INGRID and ND280 detectors	43
2. The INGRID beam direction measurement	44
3. ND280 measurements	44
4. Potential ND280 upgrades	49
C. Intermediate water Cherenkov detectors	50
1. The TITUS water Cherenkov detector	51

2. The ν PRISM detector	54
V. Physics Sensitivities	56
A. Overview	56
B. Expected observables at Hyper-K	58
C. Analysis method	61
D. Expected sensitivity to CP violation	63
E. Sensitivity to Δm_{32}^2 and $\sin^2 \theta_{23}$	67
F. Combination with atmospheric neutrino data	69
G. Summary	72
References	72

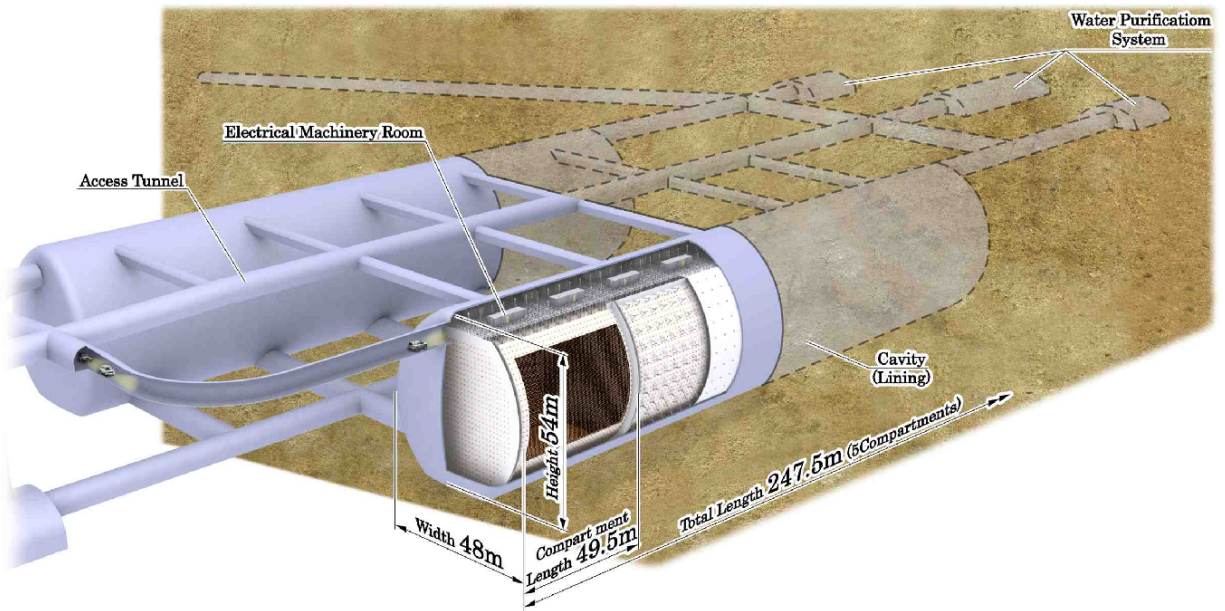


FIG. 1. Schematic view of the Hyper-Kamiokande detector [1].

I. INTRODUCTION

The goal of particle physics is to discover and understand the fundamental laws of nature. The Standard Model (SM), which is the current paradigm of elementary particles and their interactions, gives a successful account of the experimental data to date [2]. Yet, deeper insights are still needed to answer more fundamental questions. For instance, why does there exist a gauge structure of $SU(3)_C \otimes SU(2)_L \otimes U(1)_Y$ among the strong, weak and electromagnetic interactions? Why is there a three generation structure of fundamental fermions and what are the origins of the masses and generation mixings of quarks and leptons? To address these questions physics beyond the SM (BSM) is required.

The discovery of neutrino oscillations by the Super-Kamiokande (Super-K) experiment in 1998 [3] opened a new window to explore BSM physics. Evidence of neutrino oscillations is one of the most convincing experimental proofs known today that shows the existence of BSM physics at work. The mixing parameters of neutrinos, though not yet fully determined, were found to be remarkably different from those of quarks, which suggests the presence of an unknown flavor symmetry waiting to be explored. The extremely small masses of neutrinos compared with those of their charged partners lead to the preferred scenario of a seesaw mechanism [4–7], in which small neutrino masses are a reflection of the ultra-high energy scale of BSM physics.

Furthermore, a theoretical framework called Leptogenesis points to the intriguing possibility that CP asymmetries related to flavor mixing among the three generations of neutrinos may have played an important role in creating the observed matter-antimatter asymmetry in the universe [8]. Therefore, to explore the full picture of neutrino masses and mixings and to observe CP asymmetry in the neutrino sector are among the most important and urgent subjects in today's elementary particle physics world.

CP asymmetry in the neutrino sector can only be seen if all the three mixing angles governing neutrino oscillations differ from zero. All three mixing angles are successfully measured with the Super-K detector. In Super-K, θ_{23} was first measured in atmospheric neutrino observations [3], θ_{12} was constrained in solar neutrino observations [9], and the evidence of non-zero θ_{13} was found in T2K [10] which used Super-K as the far detector. In 2013, T2K established $\nu_\mu \rightarrow \nu_e$ oscillation with 7.3σ significance, leading the way towards CP violation measurements in neutrinos [11]. The great success of Super-K leads the prospect for Hyper-Kamiokande (Hyper-K) to discover CP violation.

Since 1970's, Grand Unified Theories (GUT or GUTs), which unify the strong and electroweak

interactions by embedding them in a larger gauge symmetry like $SU(5)$, have been extensively developed. Because leptons and quarks are often placed in the same multiplets, most GUTs allow baryon number violating interactions [12–14]. Baryon number violating nucleon decays would constitute an extremely sensitive probe of BSM physics and the search for such a signal remains one of the major endeavors in high energy physics. Search for nucleon decays is one of the most important physics objectives of Hyper-K.

A. Introduction to Neutrino Oscillations and CP violation

Unless otherwise stated, throughout this document, we consider the standard three flavor neutrino framework. The 3×3 unitary matrix U which describes the mixing of neutrinos [15] corresponding to the Cabbibo-Kobayashi-Maskawa matrix [16, 17] in the quark sector — often referred to as the Maki-Nakagawa-Sakata-Pontecorvo (MNSP) or Maki-Nakagawa-Sakata (MNS) [15, 18] matrix — relates the flavor and mass eigenstates of neutrinos as

$$\nu_\alpha = \sum_{i=1}^3 U_{\alpha i} \nu_i, \quad (\alpha = e, \mu, \tau), \quad (1)$$

where $\nu_\alpha (\alpha = e, \mu, \tau)$ and $\nu_i (i = 1, 2, 3)$ denote, respectively, flavor and mass eigenstates of neutrinos. Using the standard parametrization, which can be found, e.g. in Ref. [2], U can be expressed as,

$$U = \begin{pmatrix} 1 & 0 & 0 \\ 0 & c_{23} & s_{23} \\ 0 & -s_{23} & c_{23} \end{pmatrix} \begin{pmatrix} c_{13} & 0 & s_{13} e^{-i\delta_{CP}} \\ 0 & 1 & 0 \\ -s_{13} e^{i\delta_{CP}} & 0 & c_{13} \end{pmatrix} \begin{pmatrix} c_{12} & s_{12} & 0 \\ -s_{12} & c_{12} & 0 \\ 0 & 0 & 1 \end{pmatrix} \times \begin{pmatrix} 1 & 0 & 0 \\ 0 & e^{i\frac{\alpha_{21}}{2}} & 0 \\ 0 & 0 & e^{i\frac{\alpha_{31}}{2}} \end{pmatrix} \quad (2)$$

where $c_{ij} \equiv \cos \theta_{ij}$, $s_{ij} \equiv \sin \theta_{ij}$, and δ_{CP} — often called Dirac CP phase —, is the Kobayashi-Maskawa type CP phase [17] in the lepton sector. On the other hand, the two phases, α_{21} and α_{31} , — often called Majorana CP phases — have physical meaning only if neutrinos are of Majorana type [19]. While the Majorana CP phases can not be observed in neutrino oscillation [20, 21], they can be probed by lepton number violating process such as neutrinoless double beta decay.

For ultrarelativistic neutrinos, the oscillation probability of $\nu_\alpha \rightarrow \nu_\beta$ ($\alpha, \beta = e, \mu, \tau$) in vacuum is given by,

$$P(\nu_\alpha \rightarrow \nu_\beta) = \left| \sum_{i=1}^3 U_{\alpha i}^* U_{\beta i} e^{-i\frac{m_i^2}{2E}L} \right|^2 \\ = \delta_{\alpha\beta} - 4 \sum_{i>j} \Re(U_{\alpha i}^* U_{\alpha j} U_{\beta i} U_{\beta j}^*) \sin^2 \left(\frac{\Delta m_{ij}^2}{4E} L \right) + 2 \sum_{i>j} \Im(U_{\alpha i}^* U_{\alpha j} U_{\beta i} U_{\beta j}^*) \sin \left(\frac{\Delta m_{ij}^2}{2E} L \right), \quad (3)$$

where E is the neutrino energy, L is the baseline, $\Delta m_{ij}^2 \equiv m_i^2 - m_j^2$ ($i, j = 1, 2, 3$) is the mass squared differences with m_i and m_j being the neutrino masses. For the CP conjugate channel, $\bar{\nu}_\alpha \rightarrow \bar{\nu}_\beta$, the same expression in Eq. (3) holds, but the matrix U is replaced by its complex conjugate (or equivalently $\delta_{CP} \rightarrow -\delta_{CP}$ in Eq. (2)), resulting in the third term in Equation 3 switching sign.

Since there are only three neutrinos, only two mass squared differences, Δm_{21}^2 and Δm_{31}^2 , for example, are independent. Therefore, for given energy and baseline, there are 6 independent parameters, namely, three mixing angles, one CP phase, and two mass squared differences, in order to describe neutrino oscillation.

Among these six parameters, θ_{12} and Δm_{21}^2 have been measured by solar [22–24] and reactor [25–27] neutrino experiments. On the other hand, θ_{23} and $|\Delta m_{32}^2|$ (only its absolute value) have been measured by atmospheric neutrino [28, 29] and accelerator neutrino experiments [30, 31]. Recently, θ_{13} is also measured by accelerator [10, 32] and reactor experiments [33–35]. The relatively large value of θ_{13} opens the window to explore the CP phase, δ_{CP} , in neutrino oscillation.

The oscillation probability from ν_μ to ν_e in accelerator experiments is expressed as follows, to the first order of the matter effect, as [36]:

$$\begin{aligned}
P(\nu_\mu \rightarrow \nu_e) = & 4c_{13}^2 s_{13}^2 s_{23}^2 \cdot \sin^2 \Delta_{31} \\
& + 8c_{13}^2 s_{12} s_{13} s_{23} (c_{12} c_{23} \cos \delta_{CP} - s_{12} s_{13} s_{23}) \cdot \cos \Delta_{32} \cdot \sin \Delta_{31} \cdot \sin \Delta_{21} \\
& - 8c_{13}^2 c_{12} c_{23} s_{12} s_{13} s_{23} \sin \delta_{CP} \cdot \sin \Delta_{32} \cdot \sin \Delta_{31} \cdot \sin \Delta_{21} \\
& + 4s_{12}^2 c_{13}^2 (c_{12}^2 c_{23}^2 + s_{12}^2 s_{23}^2 s_{13}^2 - 2c_{12} c_{23} s_{12} s_{23} s_{13} \cos \delta_{CP}) \cdot \sin^2 \Delta_{21} \\
& - 8c_{13}^2 s_{13}^2 s_{23}^2 \cdot \frac{aL}{4E_\nu} (1 - 2s_{13}^2) \cdot \cos \Delta_{32} \cdot \sin \Delta_{31} \\
& + 8c_{13}^2 s_{13}^2 s_{23}^2 \frac{a}{\Delta m_{31}^2} (1 - 2s_{13}^2) \cdot \sin^2 \Delta_{31}, \tag{4}
\end{aligned}$$

where Δ_{ij} is $\Delta m_{ij}^2 L / 4E_\nu$, and $a[\text{eV}^2] = 7.56 \times 10^{-5} \times \rho[\text{g}/\text{cm}^3] \times E_\nu[\text{GeV}]$. The parameter δ_{CP} is the complex phase that induces the violation of CP symmetry. The corresponding probability for $\bar{\nu}_\mu \rightarrow \bar{\nu}_e$ transition is obtained by replacing $\delta_{CP} \rightarrow -\delta_{CP}$ and $a \rightarrow -a$. The third term, containing $\sin \delta_{CP}$, is the CP violating term which flips sign between ν and $\bar{\nu}$ and thus introduces CP asymmetry if $\sin \delta_{CP}$ is non-zero. The last two terms are due to the *matter effect* caused by coherent forward scattering in matter, they produce an asymmetry between neutrinos and antineutrinos unrelated to CP violation. As seen from the definition of a , the amount of asymmetry due to the matter effect is proportional to the neutrino energy at a fixed value of L/E_ν .

When we measure θ_{23} with the survival probability $P(\nu_\mu \rightarrow \nu_\mu)$ proportional to $\sin^2 2\theta_{23}$ in the first order, there is an octant ambiguity: either $\theta_{23} \leq 45^\circ$ (in the first octant) or $\theta_{23} > 45^\circ$ (in the

second octant). By combining the measurement of $P(\nu_\mu \rightarrow \nu_e)$, the θ_{23} octant can be determined.

The magnitude of the CP violation in neutrino oscillation can be characterized by the probabilities between neutrino and anti-neutrino channels, which, in vacuum, is given by [37, 38],

$$\Delta P_{\alpha\beta} \equiv P(\nu_\alpha \rightarrow \nu_\beta) - P(\bar{\nu}_\alpha \rightarrow \bar{\nu}_\beta) = 16J_{\alpha\beta} \sin \Delta_{12} \sin \Delta_{23} \sin \Delta_{31}, \quad (5)$$

and

$$J_{\alpha\beta} \equiv \Im(U_{\alpha 1} U_{\alpha 2}^* U_{\beta 1}^* U_{\beta 2}) = \pm J_{CP}, \quad J_{CP} \equiv s_{12} c_{12} s_{23} c_{23} s_{13} c_{13}^2 \sin \delta_{CP} \quad (6)$$

with positive (negative) sign for (anti-)cyclic permutation of the flavor indices e , μ and τ . The parameter J_{CP} is the lepton analogue of the CP-invariant factor for quarks, the unique and phase-convention-independent measure for CP violation [39]. In matter with constant density, the same expressions in Eqs. (3)-(6) hold but mixing angles θ_{ij} and Δm_{ij}^2 must be replaced by the effective ones in matter. Using the current best fitted values of mixing parameters, $J_{CP} \simeq 0.027 \sin \delta_{CP}$, or

$$\Delta P_{\alpha\beta} \simeq \pm 0.43 \sin \delta_{CP} \sin \Delta_{12} \sin \Delta_{23} \sin \Delta_{31}. \quad (7)$$

B. Expected results from T2K, NO ν A and reactor experiments

Regarding the third mixing angle θ_{13} , the T2K experiment [10] first found the oscillation from $\nu_\mu \rightarrow \nu_e$ as the evidence of non-zero value of θ_{13} . Following the result, the reactor experiments measure θ_{13} precisely and determined to be $\sin^2 2\theta_{13}$ to be 0.095 ± 0.01 [2]. Then, in 2013, T2K established $\nu_\mu \rightarrow \nu_e$ oscillation with 7.3σ significance, by which a measurement of CP violation in neutrinos becomes realistic.

The T2K experiment is based on a neutrino beam (mainly ν_μ) generated at J-PARC from a 30 GeV proton beam incident on a 90 cm long carbon target. The neutrino beam is observed in a 2.5° off-axis direction so that the average neutrino energy E_ν is peaked at the first oscillation maximum, with a multi purpose detector (ND280) consisting of a fully active tracker for charged particles and lead-scintillator calorimeters for photons, immersed in a 0.2-T magnetic field; it is used for characterizing the initial beam composition and flux and determining relevant cross sections. The far detector, Super-K located 295 km away in the Kamioka mine also sits 2.5° off-axis.

An on-axis detector made of iron-scintillator tracker modules is used to monitor the beam direction and profile on a daily basis. T2K has been approved for 7.8×10^{21} protons-on-target (POT). It has been running at 240 kW beam power for now, but the J-PARC upgrade plan for

the Main Ring accelerator (MR) calls for operation at 750kW by FY 2017. Hence by 2020, one expects to have accumulated the approved POT.

The NO ν A experiment at Fermilab, is also exploiting an off-axis beam from the existing Main Injector 120 GeV, initially starting at 350 kW. With the upgrades already in place, 500 kW is supposed to be possible. With additional upgrades to the Booster, 700 kW becomes possible. Both near and far detectors are identical liquid scintillator tracking calorimeters with wavelength shifter read out, respectively 330 tons and 14,000 tons. The near detector is at 1.01km while the far detector is at 810 km. The 14 mrad off-axis angle is chosen so that the $\langle E_\nu \rangle$ is 2 GeV, centered on the first oscillation maximum for ν_μ to ν_e oscillation (400 km/GeV). T2K is fully operational while NO ν A is in the process of ramping up data taking and will be fully operational in the summer 2014.

The updated physics goals for T2K are focused on the search for evidence of CP violation in the MNS mixing matrix. Combining the value of θ_{13} obtained from the reactor experiments like Daya Bay, RENO and Double Chooz which are not sensitive to the CP violation phases with those obtained from ν_e appearance which are highly correlated to the CP phases, T2K will search for:

- Signal of a CP violation phase
- Precision measurement of the MNSP mixing matrix elements Δm_{32}^2 to 10^{-4} eV^2 , $\sin^2 2\theta_{23}$ to 0.01, determination of the θ_{23} octant
- Provide experimental data useful to improve the mass hierarchy (the sign of Δm_{32}^2) sensitivity of other experiments.

The goals of NO ν A are similar but because of the longer baseline, NO ν A has more sensitivity to the mass hierarchy through the matter oscillation terms.

The two experiments, T2K and NO ν A, are complementary and a combined analysis will produce the best chances of observing δ_{CP} , the sign of Δm_{32}^2 and θ_{23} octant. Referring to the expression for the appearance probability, one notes the strong correlations between the three quantities δ_{CP} , $\sin^2 \theta_{23}$ and Δm_{32}^2 . Recent T2K and NO ν A combined analyses together with the precise θ_{13} values by reactor experiments indicate that by 2020 one could establish the presence of a CP phase at the 1.5 to 2.5 sigma level, the sign of Δm_{32}^2 at the 1 to 3 sigma level and the θ_{23} octant at the 1.5 to 2 sigma level if $|\theta_{23} - 45^\circ| > 4^\circ$ [40]. In Table I, we summarize the expected sensitivity of T2K and NO ν A for the CP phase, the sign of Δm_{32}^2 and the θ_{23} octant by 2020 together with the

TABLE I. The expected sensitivity of T2K and NO ν A for the CP phase, the sign of Δm_{32}^2 and the θ_{23} octant by 2020. As a reference, the current knowledge of neutrino oscillation parameters in PDG 2012 [2] and the 1σ range calculated by a global fit [41] in the case of $\Delta m_{32}^2 > 0$ are listed.

Parameter	T2K & NO ν A in 2020	PDG 2012	1σ range by a global fit
δ_{CP}	$\neq 0$ at $1.5 \sim 2.5 \sigma$ if $\delta_{CP} = 1.5\pi$	unknown	$1.12\pi \sim 1.72\pi$
$sign(\Delta m_{32}^2)$	determination at $1.5 \sim 3 \sigma$	unknown	unknown
$ \Delta m_{32}^2 $ (eV 2)	$\pm 0.04 \times 10^{-3}$	$(2.32^{+0.12}_{-0.08}) \times 10^{-3}$	$(2.38 \sim 2.52) \times 10^{-3}$
Δm_{21}^2 (eV 2)	not sensitive	$(7.5 \pm 0.20) \times 10^{-5}$	$(7.32 \sim 7.80) \times 10^{-5}$
θ_{23} octant	determination at $1.5 \sim 2 \sigma$ if $ \theta_{23} - 45^\circ > 4^\circ$	unknown	$< 45^\circ$
$\sin^2 2\theta_{23}$	± 0.05	> 0.95	$0.96 \sim 0.99$
$\sin^2 2\theta_{12}$	not sensitive	0.857 ± 0.024	$0.83 \sim 0.88$
$\sin^2 2\theta_{13}$	not precise	0.095 ± 0.010	$0.085 \sim 0.100$

current knowledge of neutrino oscillation parameters in Particle Data Book (PDG) 2012 [2] and the 1σ range calculated by a global fit [41].

The reactor neutrino oscillation experiments are an alternative and complementary way to measure the θ_{13} angle. Currently three experiments, Daya Bay [35] in China, Double Chooz [33] in France and RENO [34] in Korea are running. All three experiments use liquid scintillator detectors, and place detectors at the optimum (far) distance for oscillation, as well as at near distances to measure the un-oscillated flux thus canceling the systematics due to the source flux uncertainty. The reaction used is inverse beta-decay, $\bar{\nu}_e p \rightarrow e^+ n$, in which the delayed neutron capture signal (typically by the Gd nuclei doped in the scintillator) follows the prompt positron signal.

The strength and complementary of the reactor experiments lie in the fact that they are pure θ_{13} measurements, since the effects of Δm_{21}^2 term, matter effect and those sensitive to CP phase are negligible at the distance of their measurements. The survival probability is directly $1 - \sin^2 2\theta_{13} \sin^2(\Delta m_{31}^2 L/4E)$, where L is the distance and E the neutrino energy. By combining this θ_{13} measurement and the accelerator ν_e appearance probability, one can have a handle on the effect of CP violation phase, as already hinted in the most recent T2K publication [11]. In the next few years, the three experiments will improve the statistical and systematic uncertainties and ultimately aim for $\sin^2 2\theta_{13}$ measurement at the level of 5% precision.

C. Vision of Neutrino Physics in the 2020s

Before Hyper-K is online (~ 2025), we expect many progresses in neutrino physics by Super-K, T2K, NO ν A, KamLAND, Double Chooz, Daya Bay, RENO experiments and cosmological observations. In addition to accelerator and reactor experiments, Super-K will provide precise measurements of neutrino oscillation parameters in atmospheric neutrino observations, and look for the mass hierarchy and the octant of θ_{23} . Cosmological observations will provide the information of neutrino masses. If KamLAND observes the neutrino-less double β decay in the next 10 years, it would be an evidence that the neutrino is a Majorana particle with the inverted mass hierarchy. Following the progress, we definitely need a new experiment to discover CP violation in neutrinos, and unambiguously to establish the mass hierarchy and θ_{23} octant. For the purposes, we propose the Hyper-K experiment with the J-PARC neutrino beam.

1. Uniqueness of Hyper-Kamiokande with the J-PARC neutrino beam

Hyper-K is a successor of Super-K and has various physics objectives listed in Table III: search for CP violation in neutrinos, precise study of neutrino oscillations including determination of mass hierarchy and θ_{23} octant, search for nucleon decay and observation of cosmic origin neutrinos. In this document, we focus on neutrino CP violation. The uniqueness of Hyper-K is listed as follows.

- The experiment will operate in the same beam line as T2K with the same off-axis configuration. The feature of the neutrino beam and the operation of the high power beam are well understood.
- The experiment will have high statistics of neutrino events thanks to the large fiducial mass and the high power J-PARC neutrino beam.
- The systemic errors are already well understood based on Super-K and T2K which makes reliable extrapolations.

With the uniqueness, Hyper-K is one of the most sensitive experiment to probe neutrino CP violation, which will be reported in this paper. A direct test of CP violation is to measure both neutrino and antineutrino appearance probabilities in a model independent way. Although the sensitivity of CP violation is relating to a determination of the mass hierarchy, the mass hierarchy could be determined by the atmospheric neutrino measurement in Hyper-K and several measurements by other experiments mentioned in the next subsection.

TABLE II. Summary of the proposed experiments in the 2020s. The “atm.” means atmospheric neutrinos, and MH means “Mass-Hierarchy”.

Experiment (Place)	ν source	Fiducial mass (kt)	Energy (MeV)	baseline (km)	physics targets
Hyper-K (Japan)	beam	560	600	295	CP, MH, θ_{23} , θ_{13} and , Δm_{32}^2
	atm.	560	$100 \sim 10^6$	$10 \sim 10,000$	MH, CP, θ_{23} and , Δm_{32}^2
LBNE (US)	beam	34	$1,000 \sim 5,000$	1300	MH, CP, θ_{23} , θ_{13} and , Δm_{32}^2
LBNO (EU)	beam	$20 \rightarrow 100$	$1,000 \sim 10,000$	2300	MH, CP , θ_{23} , θ_{13} and , Δm_{32}^2
JUNO (China)	reactor	20	$1 \sim 10$	~ 50	MH, θ_{12} , Δm_{21}^2 , Δm_{31}^2
RENO50 (Korea)	reactor	10	$1 \sim 10$	47	MH, θ_{12} , Δm_{21}^2 , Δm_{31}^2
PINGU (South pole)	atm.	$\sim 6,000$	$1,000 \sim 10^6$	$10 \sim 10,000$	MH, θ_{23} and , Δm_{32}^2
ORCA (EU)	atm.	$\sim 2,000$	$1,000 \sim 10^6$	$10 \sim 10,000$	MH, θ_{23} and , Δm_{32}^2
INO (India)	atm.	50	$1,000 \sim 10^6$	$10 \sim 10,000$	MH, θ_{23} and , Δm_{32}^2

2. Other planned experiments: LBNE, LBNO and others

Several new experiments throughout the world are proposed to start taking data in the 2020s. The LBNE experiment in US and the LBNO experiment in Europe are accelerator based experiments to study CP violation, the mass hierarchy and neutrino oscillations precisely. The projected neutrino beam powers are ~ 1 MW, similar to J-PARC. They adopt a longer baseline than that of Hyper-K which results in the better sensitivity for the mass hierarchy thanks to the larger matter effect. Their far detectors are Liquid Ar TPCs, which require intense R&D to realize large scale detectors of $O(10)$ kton, while the technology for water Cherenkov detectors of $O(100)$ kton is more established for Hyper-K. In addition to the technology, the understanding of detector systematic is more advanced for water Cherenkov detectors. The much smaller far detectors of LBNO and LBNE result in less statistics of neutrino events. Due to the larger statistics, the better understanding of systematics and smaller matter effects relative to CP violating effects, Hyper-K has better sensitivity for CP violation.

The next generation reactor neutrino experiments, JUNO in China and RENO50 in Korea, are proposed. The main purpose of these experiments are to determine the mass hierarchy. The CP violation sensitivity in Hyper-K is greatly improved with knowledge of the mass hierarchy. The atmospheric neutrino experiments, PINGU, ORCA and INO, also focus on the mass hierarchy, and their measurements would represent a positive synergy for Hyper-K.

TABLE III. Physics targets and expected sensitivities of the Hyper-Kamiokande experiment.

Physics Target	Sensitivity	Conditions
Neutrino study w/ J-PARC ν		7.5 MW \times 10^7 sec
– CP phase precision	$< 19^\circ$	@ $\sin^2 2\theta_{13} = 0.1$, mass hierarchy known
– CPV discovery coverage	76% (3σ), 58% (5σ)	@ $\sin^2 2\theta_{13} = 0.1$, mass hierarchy known
Atmospheric neutrino study		10 years observation
– MH determination	$> 3\sigma$ CL	@ $0.4 < \sin^2 \theta_{23}$
– θ_{23} octant determination	$> 3\sigma$ CL	@ $\sin^2 2\theta_{23} < 0.99$
Nucleon Decay Searches		10 years data
– $p \rightarrow e^+ + \pi^0$	1.3×10^{35} yrs (90% CL) 5.7×10^{34} yrs (3σ CL)	
– $p \rightarrow \bar{\nu} + K^+$	3.2×10^{34} yrs (90% CL) 1.2×10^{34} yrs (3σ CL)	
Astrophysical neutrino sources		
– ^8B ν from Sun	200 ν 's / day	7.0 MeV threshold (total energy) w/ osc.
– Supernova burst ν	170,000~260,000 ν 's 30~50 ν 's	@ Galactic center (10 kpc) @ M31 (Andromeda galaxy)
– Supernova relic ν	830 ν 's / 10 years	
– WIMP annihilation at Sun		5 years observation
(σ_{SD} : WIMP-proton spin dependent cross section)	$\sigma_{SD} = 10^{-39}\text{cm}^2$ $\sigma_{SD} = 10^{-40}\text{cm}^2$	@ $M_{\text{WIMP}} = 10$ GeV, $\chi\chi \rightarrow b\bar{b}$ dominant @ $M_{\text{WIMP}} = 100$ GeV, $\chi\chi \rightarrow W^+W^-$ dominant

In Table II, the summary of the proposed experiments in the 2020s is listed with Hyper-K.

D. Overall Science goals of the Hype-Kamiokande project

In addition to the long baseline neutrino oscillation experiment that is the main focus of this document, Hyper-K will provide rich programs in a wide range of science [1]. The scope of the project includes observation of atmospheric and solar neutrinos, proton decays, and neutrinos from other astrophysical origins. The physics potential of Hyper-K is summarized in Table III.

II. THE HYPER-KAMIOKANDE DETECTOR

Hyper-Kamiokande is to be the third generation water Cherenkov detector in Kamioka, designed for neutrino studies and nucleon decay searches. Its total (fiducial) water mass of one (0.56) million tons would be approximately 20 (25) times larger than that of Super-Kamiokande. Table IV summarizes the baseline design parameters of the Hyper-K detector. The design of the detector is briefly summarized in this section.

TABLE IV. Parameters of the Hyper-Kamiokande baseline design.

Detector type		Ring-imaging water Cherenkov detector
Candidate site	Address	Tochibora mine Kamioka town, Gifu, JAPAN
	Lat.	$36^{\circ}21'20.105''\text{N}$ [†]
	Long.	$137^{\circ}18'49.137''\text{E}$ [†]
	Alt.	508 m
	Overburden	648 m rock (1,750 m water equivalent)
	Cosmic Ray Muon flux	$\sim 8 \times 10^{-7} \text{ sec}^{-1} \text{ cm}^{-2}$
	Off-axis angle for the J-PARC ν	2.5° (same as Super-Kamiokande)
	Distance from the J-PARC	295 km (same as Super-Kamiokande)
Detector geometry	Total Water Mass	0.99 Megaton
	Inner Detector (Fiducial) Mass	0.74 (0.56) Megaton
	Outer Detector Mass	0.2 Megaton
Photo-multiplier Tubes	Inner detector	99,000 20-inch ϕ PMTs 20% photo-coverage
	Outer detector	25,000 8-inch ϕ PMTs
Water quality	light attenuation length	$> 100 \text{ m @ } 400 \text{ nm}$
	Rn concentration	$< 1 \text{ mBq/m}^3$

[†] World geographical coordination system

A. Site, caverns, and tanks

The Hyper-K detector candidate site, located 8 km south of Super-K, is in the Tochibora mine of the Kamioka Mining and Smelting Company, near Kamioka town in Gifu Prefecture, Japan, as shown in Fig. 2. The J-PARC neutrino beamline is designed so that the existing Super-Kamiokande

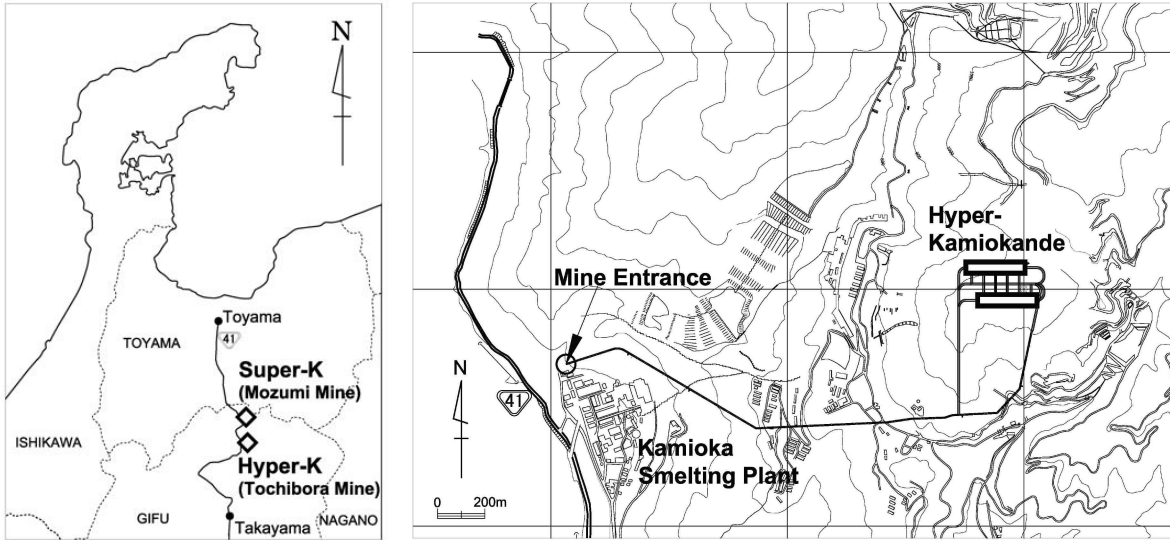


FIG. 2. The candidate site map. The site is located 8 km south of the Super-K site as shown in the left panel. The map of the Tochibora mine is shown in the right panel.

detector and the Hyper-K candidate site in Tochibora mine have the same off-axis angle. The experiment site is accessible via a drive-in, ~ 2.6 km long, (nominally) horizontal mine tunnel. The detector will lie under the peak of Nijuugo-yama, with an overburden of 648 meters of rock or 1,750 meters-water-equivalent (m.w.e.).

The rock wall in the existing tunnels and sampled bore-hole cores are dominated by Hornblende Biotite Gneiss and Migmatite in the state of sound, intact rock mass. This is desirable for constructing such unprecedented large underground cavities. The site has a neighboring mountain, Maru-yama, just 2.3 km away, whose collapsed peak enables us to dispose of more than one million m^3 of waste rock from the detector cavern excavation. Based on the in-situ measurements of the rock quality and the rock stress, it is confirmed that the Hyper-K caverns can be constructed with the existing excavation techniques.

The Mozumi mine under Mt. Ikeno-yama, where the Super-K detector is located, is another candidate site which can provide more overburden (≥ 700 m) than the Tochibora site and reduced background levels for low-energy physics, such as solar neutrinos and supernova relic neutrinos. The geological surveys have been carried out at a vicinity of the candidate site, and detailed stability analyses of the cavern construction and evaluation of the construction period and cost are in progress.

In the baseline design, the Hyper-K detector is composed of two separated caverns as shown in Fig. 1, each having an egg-shape cross section 48 meters wide, 54 meters tall, and 250 meters

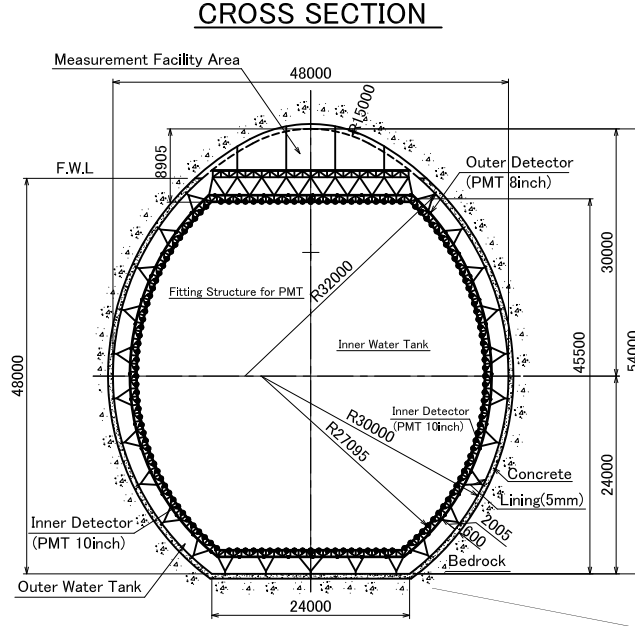


FIG. 3. Cross section view of the Hyper-Kamiokande detector.

long as shown in Fig. 3 and 4. The welded polyethylene tanks are filled up to a depth of 48 m with ultra-pure water: the total water mass equals 0.99 million tons. Detailed design of water containment system, e.g. concrete layers, polyethylene lining, and water leak detection/drainage system, has been established. Polyethylene lining sheet has been tested for pressure, tensile shear and tensile creep, and the polyethylene lining has been confirmed to have enough performance for Hyper-K.

Each tank will be optically separated by segmentation walls located every 49.5 m to form 5 (in total 10) compartments as shown in Fig. 4, such that event triggering and event reconstruction can be performed in each compartment separately and independently. Because the compartment dimension of 50 m is comparable with that of Super-K (36 m) and is shorter than the typical light attenuation length in water achieved by the Super-K water filtration system (> 100 m @ 400 nm), we expect that the detector performance of Hyper-K will be basically the same as that of Super-K. The water in each compartment is further optically separated into three regions. The inner region has a barrel shape of 42 m in height and width, and 48.5 m in length, and is viewed by an inward-facing array of 20-inch diameter photomultiplier tubes (PMTs). The entire array consists of 99,000 Hamamatsu R3600 PMTs, uniformly surrounding the region and giving a photocathode coverage of 20%. The PMT type, size, and number density are subject to optimization. An outer region completely surrounds the 5 (in total 10) inner regions and is equipped with 25,000 8-inch diameter PMTs. This region is 2 m thick at top, bottom, and barrel sides, except at both ends of

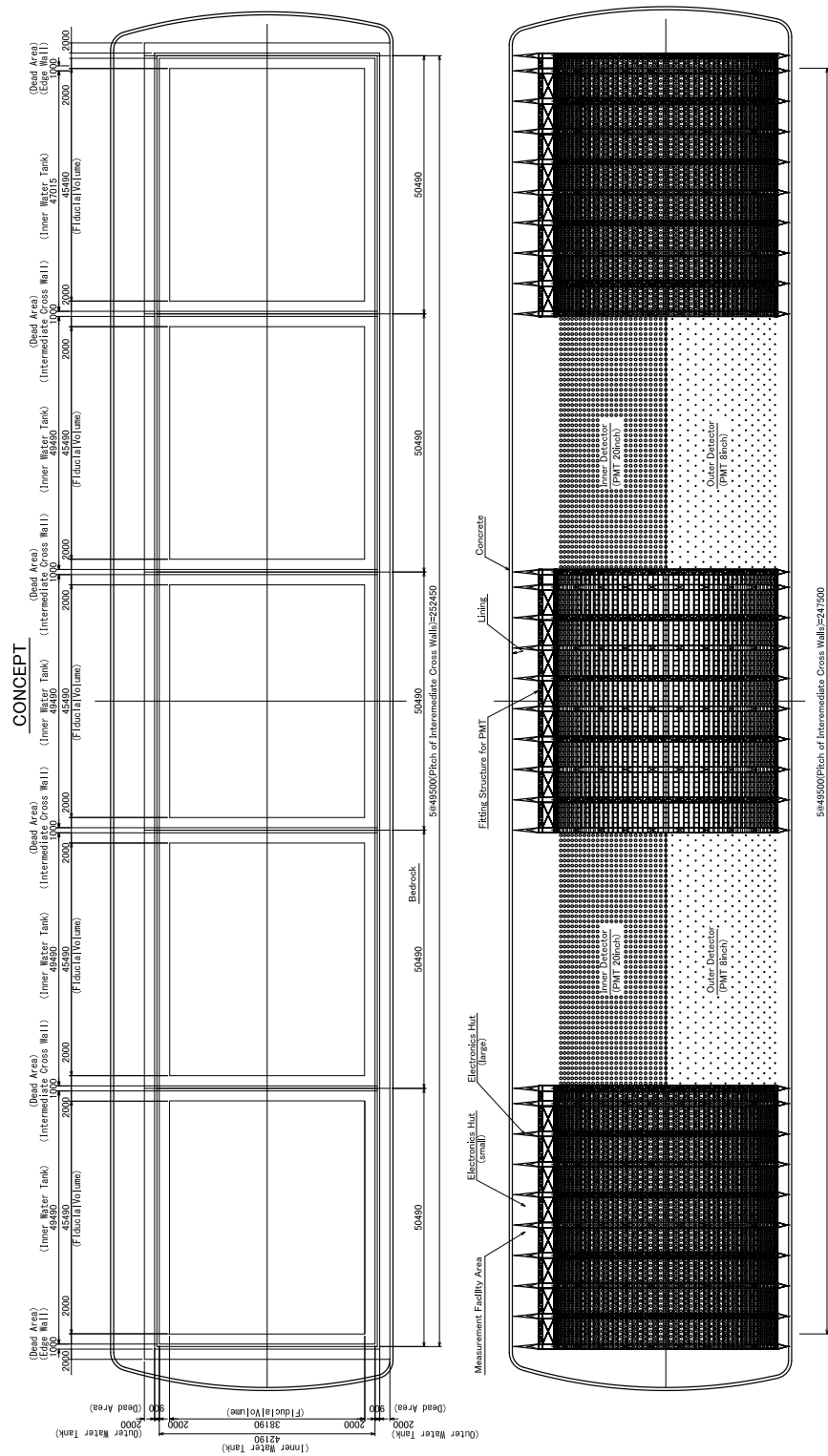


FIG. 4. Profile of the Hyper-K detector. The left panel shows the detector segmentation. The right panel shows PMT arrays and the support structure for the inner and outer detectors. Each quasi-cylindrical tank lying horizontally is segmented by intermediate walls into five compartments.

each cavern, where the outer region is larger than 2 m due to rock engineering considerations. A primary function of the outer detector is to reject entering cosmic-ray muon backgrounds and to help in identifying nucleon decays and neutrino interactions occurring in the inner detector. The middle region or dead space is an uninstrumented, 0.9 m thick shell between the inner and outer detector volumes where the stainless steel PMT support structure is located. Borders of both inner and the outer regions are lined with opaque sheets. This dead space, along with the outer region, acts as a shield against radioactivity from the surrounding rock. The total water mass of the inner region is 0.74 million tons and the total fiducial mass is 10 times $0.056 = 0.56$ million tons. The fiducial volume is defined as the region formed by a virtual boundary located 2 m away from the inner PMT plane.

The estimated cosmic-ray muon rate around the Hyper-K detector candidate site is $\sim 8 \times 10^{-7} \text{ sec}^{-1}\text{cm}^{-2}$ which is roughly 5 times larger than the flux at Super-K's location ($\sim 1.5 \times 10^{-7} \text{ sec}^{-1}\text{cm}^{-2}$). The expected deadtime due to these muons is less than 1% and negligible for long baseline experiments, as well as nucleon decay searches and atmospheric neutrino studies.

B. Water purification system

Water is the target material and signal-sensitive medium of the detector, and thus its quality directly affects the physics sensitivity. In order to realize such a huge Cherenkov detector, achieving good water transparency is the highest priority. In addition, as radon emanating from the photosensors and detector structure materials is the main background source for low energy neutrino studies, an efficient radon removal system is indispensable.

In Super-Kamiokande the water purification system has been continually modified and improved over the two-decade course of SK-I to SK-IV. As a result, the transparency is now kept above 100 m and is very stable, and the radon concentration in the tank is held below 1 mBq/m^3 . Following this success, the Hyper-Kamiokande water system design will be based on the current Super-Kamiokande water system.

Naturally, ever-faster water circulation is generally more effective when trying to keep huge amounts of water clean and clear, but increasing costs limit this straightforward approach so a compromise between transparency and recirculation rate must be found. In Super-Kamiokande, 50,000 tons of water is processed at the rate of 60 tons/hour in order to keep the water transparency (the attenuation length for 400–500 nm photons) above 100 m, and 20 m^3 /hour of radon free air is generated for use as a purge gas in degas modules, and as gas blankets for both buffer tanks and

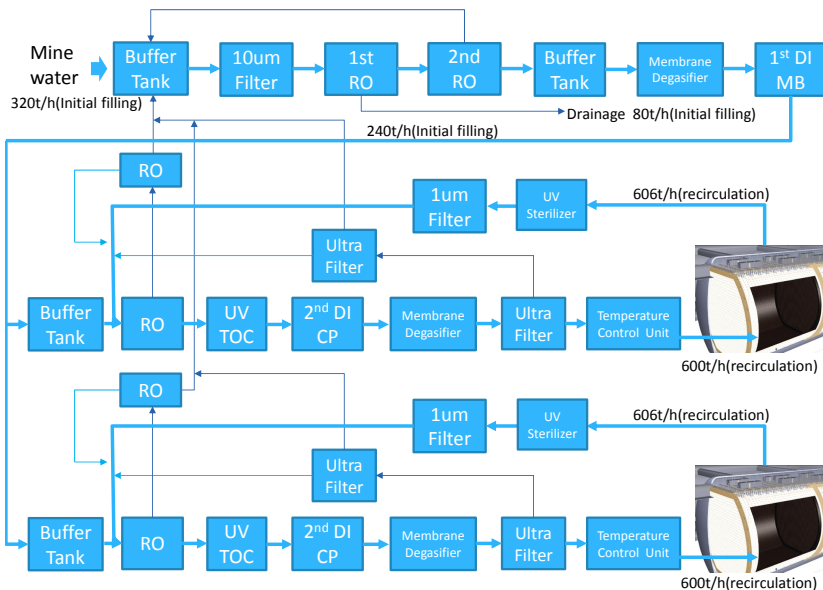


FIG. 5. The water flow design of the Hyper-Kamiokande water system.

the Super-Kamiokande tank itself. For the 0.99 million tons of water in Hyper-Kamiokande, these process speeds will need to be scaled-up to $1200 \text{ m}^3/\text{hour}$ for water circulation and $400 \text{ m}^3/\text{hour}$ for radon free air generation.

Figure 5 shows the current design of the Hyper-Kamiokande water purification system. With these systems, the water quality in Hyper-Kamiokande is expected to be same as that in Super-Kamiokande.

Adding dissolved gadolinium sulfate for efficient tagging of neutrons has been studied as an option to enhance Hyper-K physics capability. The feasibility of adding Gd to Super-K is now under study with EGADS (Evaluating Gadolinium's Action on Detector Systems) project in Kamioka. We have been careful to keep the possibility of gadolinium loading in mind when designing the overall Hyper-Kamiokande water system.

C. Photosensors

In order to achieve a broad scientific goals of Hyper-K, particles with a wide range of energy need to be reconstructed. Depending on the energy of particle that emits Cherenkov photons, the number of photons that hit each photosensor ranges from one to several hundred. Thus, the photosensors are required to have a wide dynamic range and good linearity. The location

Shape	Hemispherical
Photocathode area	50 cm diameter
Quantum efficiency	22 % at $\lambda = 390$ nm
Dynodes	11 stage Venetian blind type
Gain	10^7 at ~ 2000 V
Dark pulse rate	3 kHz at 10^7 gain
Transit time	90 nsec at 10^7 gain
Transit time spread	2.2 nsec (1σ) for single photoelectron signals
Weight	13 kg
Pressure tolerance	6 kg/cm ² water proof

TABLE V. Specifications of the 20-inch PMT (Hamamatsu R3600).

of the interaction vertex is reconstructed using Cherenkov photon arrival timing information at each PMT. Therefore, good timing resolution of the photosensors is essential, and the jitter of the transit time is required to be less than 3 nsec (1σ) for a single photon.

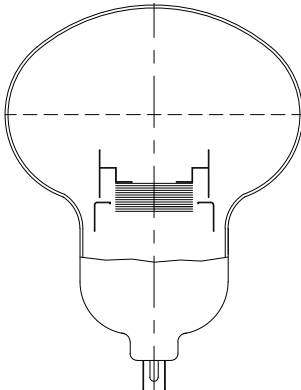
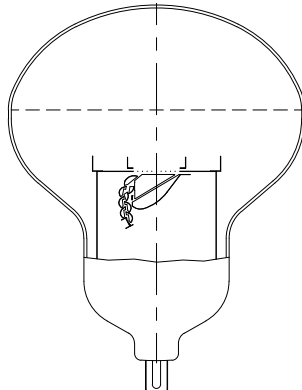
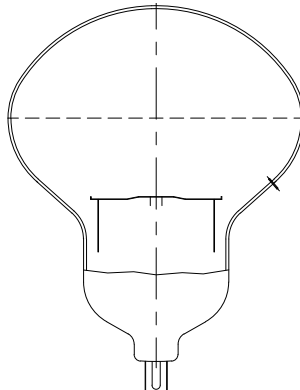
In the baseline design, we have selected the 20-inch diameter PMT (Hamamatsu R3600) used successfully in Super-K as the primary sensor candidate for the Hyper-K inner detector. The R3600 is already known to satisfy the requirements above. Moreover, it has been operated for more than 15 years in Super-K and thus the long-term stability is well understood. The specifications of the 20-inch PMT is summarized in TABLE V. The total number of the inner detector PMTs in Hyper-K will be about 99,000.

For the outer detector, we have selected the same design as that of the Super-K outer detector. The photosensors are Hamamatsu R1408 PMTs with an 8-inch diameter photocathode. A total of 25,000 these PMTs cover 1% of the inner wall of the outer detector. Like Super-K, an acrylic wavelength shifting plate of dimensions 60 cm \times 60 cm is placed around the bulb of each of the 8-inch PMTs to increase the photon detection efficiency.

In order to further improve the performance and reduce the cost from the baseline design, we have been developing new photosensors as possible alternative options to R3600.

Two types of new 20-inch sensors have been developed in cooperation with Hamamatsu Photonics, K. K. One is a hybrid photo-detector (HPD), which uses an avalanche diode instead of a metal dynode for the multiplication of photoelectrons emitted from a photocathode. The other option is a PMT with a box-and-line dynode, which has a faster time response and a better col-

TABLE VI. Specification of three 20-inch diameter photosensors, which are candidates for Hyper-K.

Type	PMT	PMT	Hybrid Photo-Detector
Amplification	Venetian blind dynode	Box-and-Line dynode	Avalanche diode
			
Model	R3600, HPK	R12860, HPK	R12850, HPK
Collection efficiency	80%	93%	95%
Transit time spread (FWHM)	5.5 nsec	2.7 nsec	0.75 nsec
Bias voltage	2 kV	2 kV	8 kV

lection efficiency compared to R3600. The specifications of three 20-inch photosensor candidates for Hyper-K are summarized in Table VI. The 8-inch HPDs are currently under test in a 200-ton water Cherenkov detector. New 20-inch sensors will be tested in near future.

As a common option for those large aperture photosensors, we have been developing a high quantum efficiency (QE) photocathode. The measured QE of eight high-QE R3600's and a typical QE of normal R3600 are shown in Fig 6.

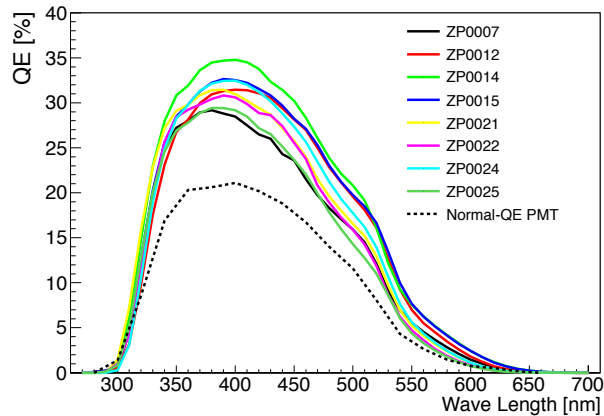


FIG. 6. Measured QE for eight high-QE R3600's (solid lines) and a normal R3600 (dashed line).

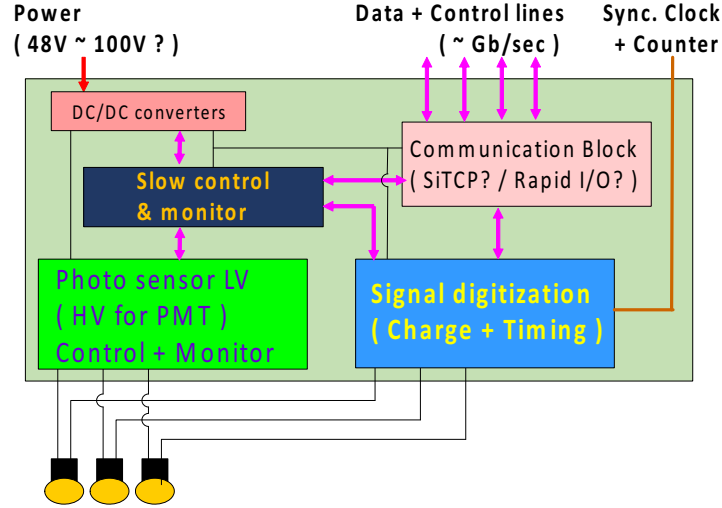


FIG. 7. Schematic diagram of the front-end module.

There are also other efforts to develop new photosensors that can be potentially used for Hyper-K including the outer detector or new near detectors, such as PMT by ETEL/ADIT and Large-Area Picosecond Photo-Detectors (LAPPD).

There have also been several attempts to improve the photon collection efficiency with special lens systems, wavelength shifters, or mirrors attached to the existing sensors. The effect of such additional system to the detector performance, such as angular acceptance and timing resolution, needs to be carefully studied.

D. Electronics and data acquisition system

In terms of the required specifications and the number of photosensors in one compartment, the current design of the Hyper-K detector is similar to that of the Super-K detector. Therefore, it is possible for us to design the data acquisition system using the same concept as SK-IV, reading out all the hit information from the photosensors, including the dark noise hits.

However, because the egg-shape of Hyper-K detector makes the cable routing and mechanical support difficult to design. We are now planning to place the front-end electronics module and the power supply for the photosensor in the detector water, close to the photosensor. The underwater front-end electronics will be enclosed in a pressure tolerant water-tight housing, which have been used in other experiments with several established techniques.

The schematic diagram of the front-end module is shown in Fig. 7. There are four main

TABLE VII. Specification of the SK-IV front-end electronics

Items	Required values
Built-in discriminator threshold	1/4 p.e (~ 0.3 mV)
Processing speed	$\sim 1\mu\text{sec. / hit}$
Charge resolution	~ 0.05 p.e. (RMS) for < 5 p.e.
Charge dynamic range	0.2 \sim 2500 pC (0.1 \sim 1250 p.e.)
Timing resolution	0.3 ns RMS (1 p.e.) < 0.3 ns RMS (> 5 p.e.)
Least significant bit resolution	0.52 ns

functional blocks in the front-end board. One module accepts signals from 24 photosensors.

The signal digitization block accepts the signals from the photosensors and convert them to the digital timing and charge data. Because of similar requirements, the SK-IV front-end electronics using the charge to time conversion (QTC) chip [42] and ATLAS Muon TDC (AMT) chip [43] is used as a reference to the baseline design. The Hyper-K front-end is required to have equal or better performance than the specification of SK-IV electronics summarized in Table VII. Because the relative timing is used to reconstruct the event vertex in the detector, all the modules have to be synchronized to the external reference clock.

The photosensor power supply block controls the photosensor voltage supply. For HPD, we suppose that a voltage supply is embedded inside its housing. If standard PMTs are used as the photosensor, the high voltage modules will be put in the same enclosure as the front-end electronics.

The slow control block controls and monitors the status of the power supply for the photosensors. Also, the voltage, the current and the temperature in the front-end module have to be monitored.

The communication block transports data from/to the other modules. In order to reduce the amount of cables, the modules will be connected to each other to make a network of data transfer line. To avoid a single point failure, a module will be equipped with several communication ports and connected to multiple modules.

The schematic diagram of the data readout and processing system is shown in Fig. 8. In the current baseline design, all the PMT signals above a certain threshold (e.g. $\sim 1/4$ photoelectrons) are digitized and read out by the computer. The expected data rate from one front-end module is $\sim 2\text{MB/sec}$ and the total data rate per compartment will be $\sim 1\text{GBytes/sec}$. Based on the experience with SK-IV, about 20 computers will be necessary to read out the data from one compartment. In order to select “events” to be transferred to the offline computers with the software trigger, ~ 10

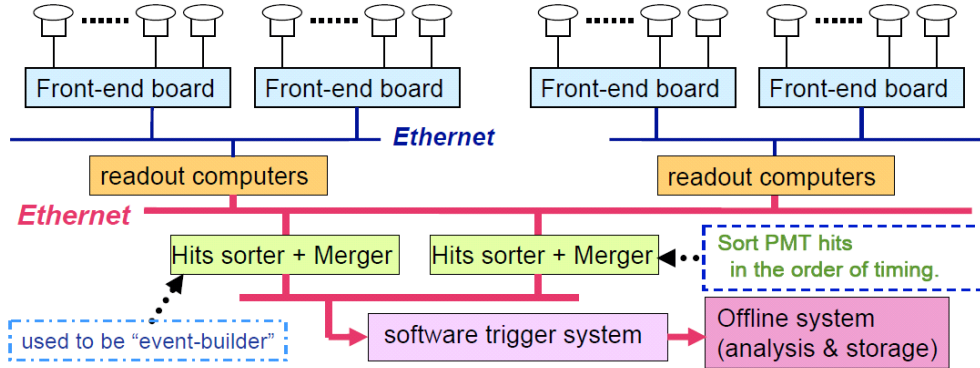


FIG. 8. Schematic diagram of data readout and processing system.

TABLE VIII. Calibration techniques used in Super-Kamiokande

Calibration source	Purpose
Nitrogen-dye laser	Timing response, charge linearity, OD
Laser with various wavelength	Water attenuation & scattering
Xe lamp + scintillator ball	PMT gain, position dependence
Deuterium-tritium (DT) fusion generator [¹⁶ N]	Low energy response
Nickel + ²⁵² Cf [Ni(<i>n</i> , γ)Ni]	Absolute gain, photo-detection efficiency
Cosmic ray muon / π^0 / decay electron	Energy calibration for high energy events

computers will be necessary.

Although the baseline design is proved to work with the Super-K experience, there are several ongoing R&D to improve the performance of the electronics/DAQ for Hyper-K. The current effort includes the development of a front-end electronics based on FADC, R&D of an FPGA-based high precision TDC, and a more intelligent trigger for low energy events and/or events extending over multiple compartments. It is planned to test multiple options with a prototype detector to evaluate their feasibility and performance.

E. Detector calibration

In order to achieve the scientific goals of Hyper-K, precise calibration of the detector is indispensable. Because the Super-K detector has been operated successfully for more than a decade

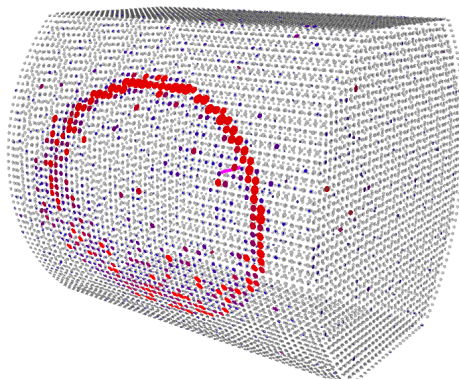


FIG. 9. An event display of simulated event by WCSim. The “egg-shape” cross section is implemented into WCSim. A muon is generated at the center of the detector and is directed to the wall direction with 500 MeV/c momentum.

with many outstanding scientific achievements, the Hyper-K detector calibration system will be designed based on the techniques established with the Super-K calibration [44].

In Super-Kamiokande, various kind of calibrations have been carried out, as summarized in Table VIII. Since in Hyper-K has ten individual compartments, it is not realistic to perform the same calibration work with the same system as Super-K. In addition, its egg-shaped cross section will make calibrations near the wall of PMTs difficult. Therefore, the detector should have dedicated, automated systems for accurately placing various calibration sources at desired positions inside the tank. Design of such deployment system is ongoing, utilizing the experience in other experiment, such as Borexino, SNO, and KamLAND, in addition to Super-K.

In parallel, R&D of advanced calibration sources, such as a light source using an LED and new neutron generators, is ongoing. Also, a facility to characterize the response of a photosensor to light with various wavelength, incident angle, and location on the sensor, is being developed to provide more detailed information that can be used to improve the detector simulation.

F. Expected detector performance

We have been developing a detector simulation dedicated to Hyper-K based on “WCSim,” [45] which is a water Cherenkov detector simulator based on the GEANT4 library [46, 47]. First, the simulation model of WCSim was validated by implementing the Super-K detector geometry in WCSim and comparing the detector responses with those by the official Super-K MC simulation

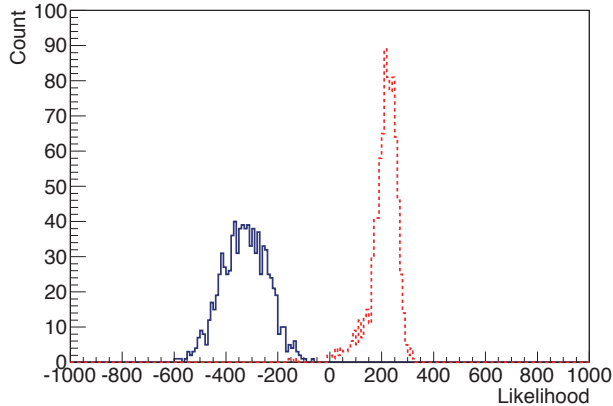


FIG. 10. PID likelihood functions for electron (blue solid histogram) and μ (red dashed histogram) with 500 MeV/ c momentum. A negative (positive) value indicates electron-like (μ -like) particle.

TABLE IX. Comparison of performance of SK-II (20% photo-coverage), SK-IV (40% photo-coverage), and the expected performance of Hyper-Kamiokande baseline design (20% photo-coverage) with preliminary Hyper-K simulation and reconstruction.

	SK-II		SK-IV		Hyper-K	
	e	μ	e	μ	e	μ
Particle type ($p = 500$ MeV/ c)						
Vertex resolution	28 cm	23 cm	25 cm	17 cm	27 cm	30 cm
Particle identification	98.5%	99.0%	98.8%	99.5%	>99.9%	99.2%
Momentum resolution	5.6%	3.6%	4.4%	2.3%	4.0%	2.6%

based on GEANT3 [48] and tuned with the Super-K data. Then, the detailed Hyper-K detector geometry has been implemented in WCSim. An example of event display is shown in Fig. 9.

A new reconstruction algorithm developed for Super-K/T2K [11], named “fitQun,” has been adopted for the Hyper-K analysis. It uses a maximum likelihood fit with charge and time probability density functions constructed for every PMT hit assuming several sets of physics variables (such as vertex, direction, momentum, and particle type). In the conventional event reconstruction in Super-K, physics variables are determined step-by-step, while fitQun can determine all physics variables at a time. In addition, fitQun uses information from not only fired PMTs but also from PMTs which are not fired, utilizing more information than the conventional method which uses only fired PMTs.

In the baseline design of Hyper-K, 20-inch PMTs cover 20% of the inner detector surface. This is the same setup as Super-K from 2002 to 2005 (SK-II period). Based on the experience with

SK-II, the effect of the photo-coverage difference between 20% and 40% is known to be small for neutrino events with energy relevant to the long baseline oscillation experiment. Therefore, the Hyper-K detector is expected to have similar performance as Super-K.

We have evaluated the expected performance of the Hyper-K detector using the MC simulation and reconstruction tools under development. Electrons and muons with 500 MeV/ c are generated with a fixed vertex (at center of the tank) and direction (toward the barrel of the tank) in the Hyper-K detector simulation, and fitQun reconstruction is applied. Figure 10 shows the likelihood function for the particle identification. A negative (positive) value indicates electron-like (μ -like) particle. It demonstrates a clear separation of electrons and muons. The obtained performance of Hyper-Kamiokande is compared with the performance of SK-II (20% photo coverage, old electronics) and SK-IV (40% photo coverage, new electronics) in Table IX. The vertex resolution for muon events will be improved to the same level as Super-K with update of the reconstruction program. From the preliminary studies, the performance of Hyper-K is similar to or possibly better than SK-II or SK-IV with the new algorithm. In the physics sensitivity study described in Section V, a Super-K full MC simulation with the SK-IV configuration is used because it includes the simulation of new electronics and tuned with the real data, while giving similar performance with Hyper-K as demonstrated above.

III. NEUTRINO BEAM AT J-PARC

This section describes the J-PARC accelerators/neutrino beamline and planned operational parameters for the design beam power of 750 kW. The work necessary to ramp up to this beam power from the current level of 240 kW is well in progress, and is to be accomplished considerably earlier than Hyper-K starts data taking. The prospects for realizing future multi-MW beam powers with the existing facility are then outlined. A state-of-the-art prediction of the neutrino flux that will be generated by the facility has been examined in detail by the current T2K experiment. This is described together with the expected uncertainties.

A. J-PARC accelerator cascade and the neutrino experimental facility

The J-PARC accelerator cascade [49] consists of a normal-conducting LINAC as an injection system, a Rapid Cycling Synchrotron (RCS), and a Main Ring synchrotron (MR). H^- ion beams, with a peak current of 50 mA and pulse width of 500 μs , are accelerated to 400 MeV by the LINAC. Conversion into a proton beam is achieved by charge-stripping foils at injection into the RCS ring, which accumulates and accelerates two proton beam bunches up to 3 GeV at a repetition rate of 25 Hz. Most of the bunches are extracted to the Materials and Life science Facility (MLF) to generate intense neutron/muon beams. The beam power of RCS extraction is rated at 1 MW. With a prescribed repetition cycle, four successive beam pulses are injected from the RCS into the MR at 40 ms ($= 1/25$ Hz) intervals to form eight bunches in a cycle, and accelerated up to 30 GeV. In fast extraction (FX) mode operation, the circulating proton beam bunches are extracted within a single turn into the neutrino primary beamline by a kicker/septum magnet system.

Fig. 11 shows an overview of the neutrino experimental facility [50]. The primary beamline guides the extracted proton beam to a production target/pion-focusing horn system in a target station (TS). The pions decay into muons and neutrinos during their flight in a 110 m-long decay volume. A graphite beam dump is installed at the end of the decay volume, and muon monitors downstream of the beam dump monitor the muon profile. A neutrino near detector complex is situated 280 m downstream of the target to monitor neutrinos at production. To generate a narrow band neutrino beam, the beamline utilizes an off-axis beam configuration [51] for the first time ever, with the capability to vary the off-axis angle in the range from 2.0° to 2.5° . The latter value has been used for the T2K experiment and is assumed also for the proposed project. The centreline of the beamline extends 295 km to the west, passing midway between Tochibora and Mozumi, so

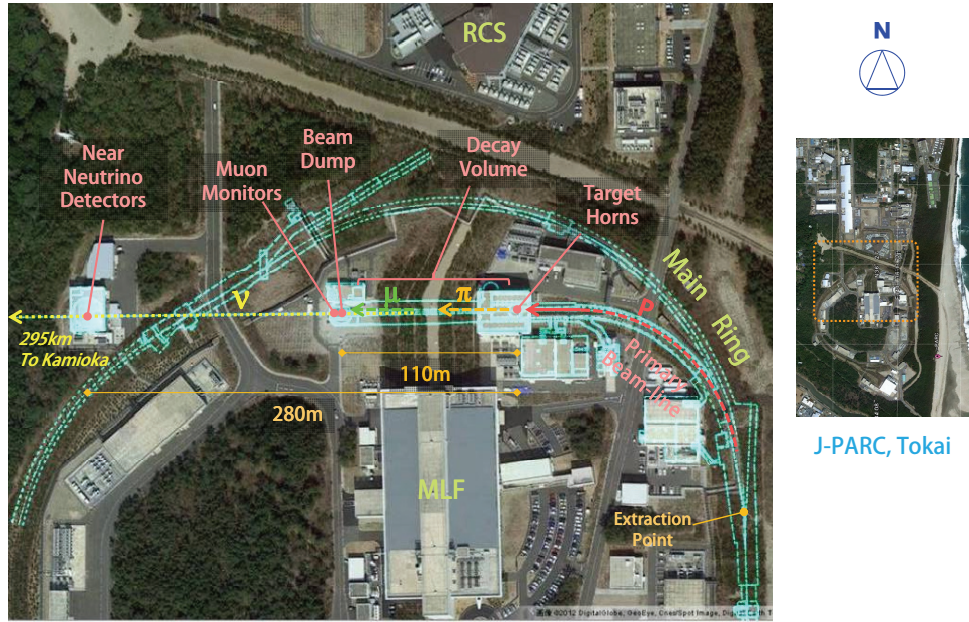


FIG. 11. The neutrino experimental facility (neutrino beamline) at J-PARC.

that both sites have identical off-axis angles.

Fig. 12 shows a cross section of the secondary beamline, and a close-up of the TS helium vessel. A helium-cooled graphite production target is inserted within the bore of the first of a three-horn pion-focusing system. At 750 kW operation, ~ 20 kW heat load is generated in the target.¹ The horns are suspended from the lid of the TS helium vessel. Each horn comprises two co-axial cylindrical conductors which carry a 320 kA pulsed current. This generates a peak toroidal magnetic field of 2.1 Tesla which focuses one sign of pions. The heat load generated in the inner conductors by secondary particles and by joule heating is removed by water spray cooling.² A helium cooled, double skin titanium alloy beam window separates the helium environment in the TS vessel (~ 1 atm pressure) from the vacuum of the primary beamline. All secondary beamline components become highly radioactive during operation and replacements require handling by a remotely controlled overhead crane in the target station. Failed targets can be replaced within horn-1 using a bespoke target installation and exchange mechanism. Both the decay volume and the beam dump dissipate $\sim 1/3$ of the total beam power, respectively. The steel walls of the decay volume and the graphite blocks of the hadron absorber (core of the beam dump) are water cooled

¹ The beam size on the target ($r = \sim 4$ mm) should be strictly controlled with beam monitors at a final focusing section of the primary beam-line, and also with an optical transition monitor (OTR)[52] in front of the target.

² Gaseous hydrogen and oxygen are generated from the cooling water by radiolysis, which could limit the beam power. A recombination catalyst is installed to prevent the risk of explosion.

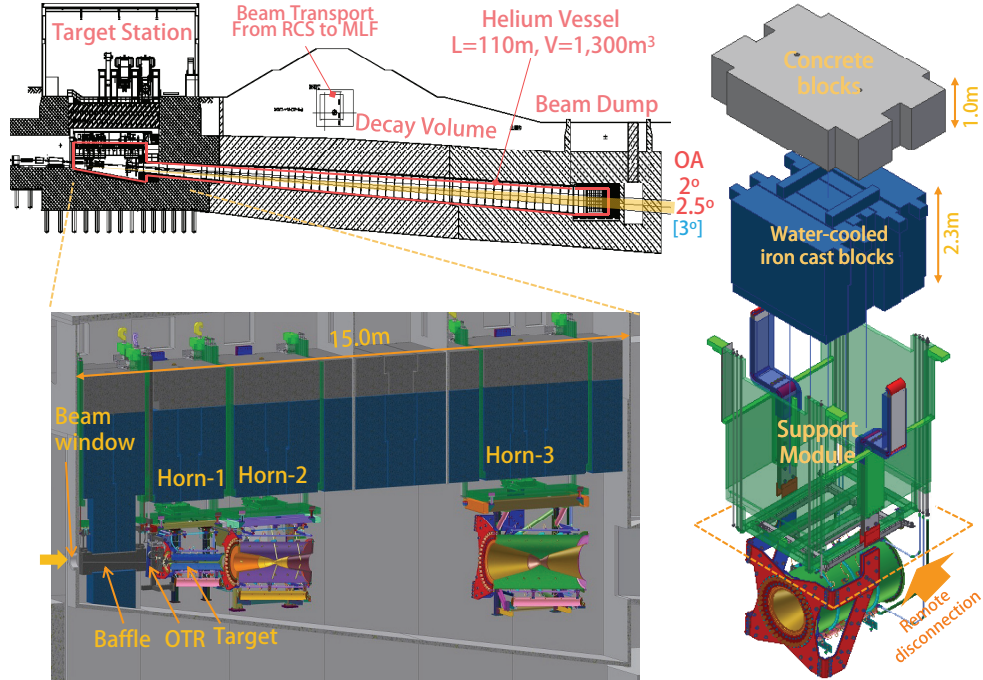


FIG. 12. (Left) Side view of the secondary beamline, with a close up of the target station helium vessel. (Right) A schematic view of a support module and shield blocks for horn-3. If a horn fails, the horn together with its support module is transferred remotely to a purpose-built maintenance area, disconnected from the support module and replaced.

and both are designed to deal with 3~4 MW beam since neither can be upgraded nor maintained after irradiation by the beam.³

B. Power upgrade of Main Ring synchrotron and the neutrino beamline

In the MR FX mode operation, so far 1.2×10^{14} ppp beam intensity has been achieved, a world record for extracted protons per pulse for any synchrotron and equating to an average beam power of 240 kW. The accelerator team is following a concrete upgrade scenario [53, 54] to reach the design power of 750 kW in forthcoming years, with a typical planned parameter set as listed in TABLE X. This will double the current repetition rate by (i) replacing the magnet power supplies, (ii) replacing the RF system, and (iii) upgrading injection/extraction devices. Furthermore, conceptual studies on how to realize 1~2 MW beam powers and even beyond are now underway [55], such as by raising the RCS top energy, enlarging the MR aperture, or inserting an “emittance-damping” ring

³ The water cooling systems in the utility buildings only have capacity for 750 kW operation, thus need to be upgraded for multi-MW beam operation.

TABLE X. Planned parameters of the J-PARC Main Ring for fast extraction. Numbers in parentheses are those achieved up until May 2013.

parameter	value	
circumference	1567.5 m	
beam kinetic energy	30 GeV	
beam intensity	2.0×10^{14} ppp ^a	(1.2×10^{14})
	2.5×10^{13} ppb	(1.5×10^{13})
[RCS equivalent power]	[600 kW]	(360)
RF frequency	1.67–1.72 MHz	
harmonic number	9	
number of bunches	8 / spill	
spill width	$\sim 5 \mu\text{s}$	
bunch full width	150– ~ 400 ns	(~ 160)
maximum RF voltage	560 kV	(280)
repetition period	1.3 sec	(2.48)
	$0.12_{\text{inj}} + 0.5_{\text{acc}} + 0.68_{\text{decel}}$	($0.14 + 1.4 + 0.94$)
beam power	750 kW	(240)

^a Most recent studies on space-charge tracking simulation show [53] that 2.3×10^{14} ppp (2.9×10^{13} ppb, equivalent to RCS 700 kW operation) is achievable by introducing 2nd harmonic RF during injection.

between the RCS and MR.

The neutrino production target and the beam window are designed for 750 kW operation with 3.3×10^{14} ppp (equivalent to RCS 1 MW operation) and 2.1 sec cycle. In the target, the pulsed beam generates an instantaneous temperature rise per pulse of 200 C° and a thermal stress wave of magnitude 7 MPa, giving a safety factor of ~ 5 against the tensile strength. Although this safety factor will be reduced by cyclic fatigue, radiation damage⁴ and oxidization of the graphite, a lifetime of 2–5 years is expected.⁵ In order to both increase lifetimes and to realize multi-MW beam operation, the beamline team intends to investigate modifications to the existing design, and even to develop a new concept that can dissipate a higher heat load and may be more resilient to radiation damage.

⁴ Graphite loses integrity at proton fluences of around 10^{22} protons/cm², which would be reached after around 5 years operation at 750 kW. The target has been designed to operate at a maximum temperature of around 700°C, which from neutron irradiation data should minimise any dimensional changes and reduction in thermal conductivity.

⁵ By adopting the double rep-rate scenario, the number of protons per pulse will be reduced, and hence the thermal shock per pulse will be reduced. However the total proton fluence on the target will be increased, thus increasing the heat load and the effects of radiation damage.

TABLE XI. Acceptable beam power and achievable parameters for each beamline component [56, 57]. Limitations as of May 2013 are also given in parentheses.

component	beam power/parameter
target	3.3×10^{14} ppp
beam window	3.3×10^{14} ppp
horn	
cooling for conductors	1.85 MW ^a
stripline cooling	1~2 MW (400 kW)
hydrogen production	1~2 MW (300 kW)
horn current	320 kA (250 kA)
power supply repetition	1 Hz (0.4 Hz)
decay volume	4 MW
hadron absorber/beam dump	3 MW
water cooling facilities	~2 MW (750 kW)
radiation shielding	4 MW (750 kW)
radioactive air leakage to the TS ground floor	~2 MW (500 kW)
radioactive cooling water treatment	~2 MW (600 kW)

^a assuming 2.0×10^{14} ppp and 0.5 sec cycle

So far the horns were operated with a 250 kA pulsed current and a minimum repetition cycle of 2.48 sec. To operate the horns at a doubled repetition rate of ~ 1 Hz requires new individual power supplies for each horn utilizing an energy recovery scheme and low inductance/resistance striplines. These upgrades will reduce the charging voltage/risk of failure, and, as another benefit, increase the pulsed current to 320 kA. The horn-1 water-spray cooling system has sufficient capacity to keep the conductor below the required 80°C at up to 1.85 MW.

Considerable experience has been gained on the path to achieving 240 kW beam power operation, and the beamline group is promoting upgrades to realize 750 kW operation, such as by improving the activated air confinement in TS, and is proposing to expand the facilities for the treatment of activated water. TABLE XI gives a summary of acceptable beam power and/or achievable parameters for each beamline component [56, 57], after the proposed upgrades in forthcoming years.

C. The neutrino flux calculation

The T2K flux [58] is estimated by simulating the J-PARC neutrino beam line while tuning the modeling of hadronic interactions using data from NA61/SHINE [59, 60] and other experiments measuring hadronic interactions on nuclei. To date, NA61/SHINE has provided measurements of pion and kaon production multiplicities for proton interactions on a 0.04 interaction length graphite target, as well as the inelastic cross section for protons on carbon. Since “thin” target data are used, the secondary interactions of hadrons inside and outside of the target are modeled using other data or scaling the NA61/SHINE data to different center of mass energies or target nuclei.

For the studies presented in this document, the T2K flux simulation has been used with the horn currents raised from 250 kA to 320 kA. The flux is estimated for both polarities of the horn fields, corresponding to neutrino enhanced and antineutrino enhanced fluxes. The calculated fluxes at Hyper-K, without oscillations, are shown in Fig. 13.

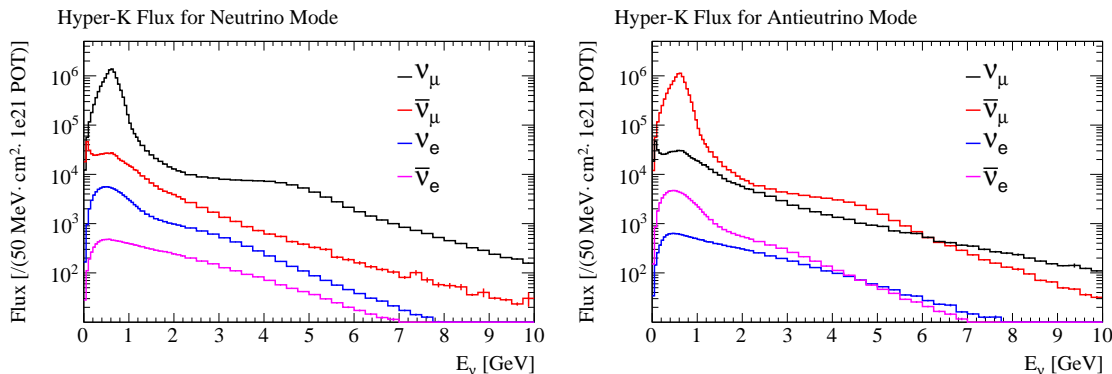


FIG. 13. The predicted Hyper-K neutrino fluxes from the J-PARC beam without oscillations. The neutrino enhanced beam is shown on the left and the antineutrino enhanced beam is shown on the right.

1. The flux uncertainties

The sources of uncertainty in the T2K flux calculation include:

- Uncertainties on the primary production of pions and kaons in proton on carbon collisions.
- Uncertainties on the secondary hadronic interactions of particles in the target or beam line materials after the initial hadronic scatter.

- Uncertainties on the properties of the proton beam incident on the target, including the absolute current and the beam profile.
- Uncertainties on the alignment of beam line components, including the target and magnetic horns.
- Uncertainties on the modeling of the horn fields, including the absolute field strength and asymmetries in the field.

The uncertainties on the hadronic interaction modeling are the largest contribution to the flux uncertainty and may be reduced by the use of replica target data. A preliminary analysis using a subset of the replica target data from NA61/SHINE has shown that it can be used to predict the T2K flux [61]. Since it is expected that replica target data will be available for future long baseline neutrino experiments, the Hyper-K flux uncertainty is estimated assuming the expected uncertainties on the measurement of particle multiplicities from the replica target. Hence, uncertainties related to the modeling of hadronic interactions inside the target are no longer relevant, however, uncertainties for interactions outside of the target are considered. The uncertainties on the measured replica target multiplicities are estimated by applying the same uncertainties that NA61/SHINE has reported for the thin target multiplicity measurements.

The total uncertainties on the flux as function of the neutrino energy are shown in Fig. 14. In oscillation measurements, the predicted flux is used in combination with measurements of the neutrino interaction rate from near detectors. Hence, it is useful to consider the uncertainty on the ratio of the flux at the far and near detectors:

$$\delta_{F/N}(E_\nu) = \delta \left(\frac{\phi_{HK}(E_\nu)}{\phi_{ND}(E_\nu)} \right) \quad (8)$$

Here $\phi_{HK}(E_\nu)$ and $\phi_{ND}(E_\nu)$ are the predicted fluxes at Hyper-K and the near detector respectively. T2K uses the ND280 off-axis detector located 280 m from the T2K target. At that distance, the beam-line appears as a line source of neutrinos, compared to a point source seen by Hyper-K, and the far-to-near ratio is not flat. For near detectors placed further away, at 1 or 2 km for example, the far-to-near flux ratio becomes more flat and there is better cancellation of the flux uncertainties between the near and far detectors. Fig. 15 shows how the uncertainty on the far-to-near ratio evolves for baselines of 280 m, 1 km and 2 km. While this extrapolation uncertainty is reduced for near detectors further from the production point, even the 280 m to Hyper-K uncertainty is less than 1% near the flux peak energy of 600 MeV.

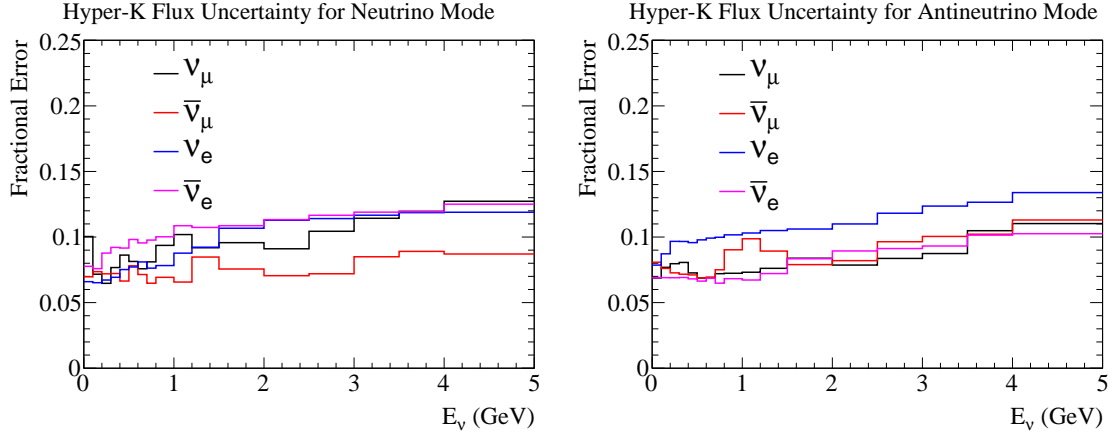


FIG. 14. The predicted uncertainty on the neutrino flux calculation assuming replica target hadron production data are available.

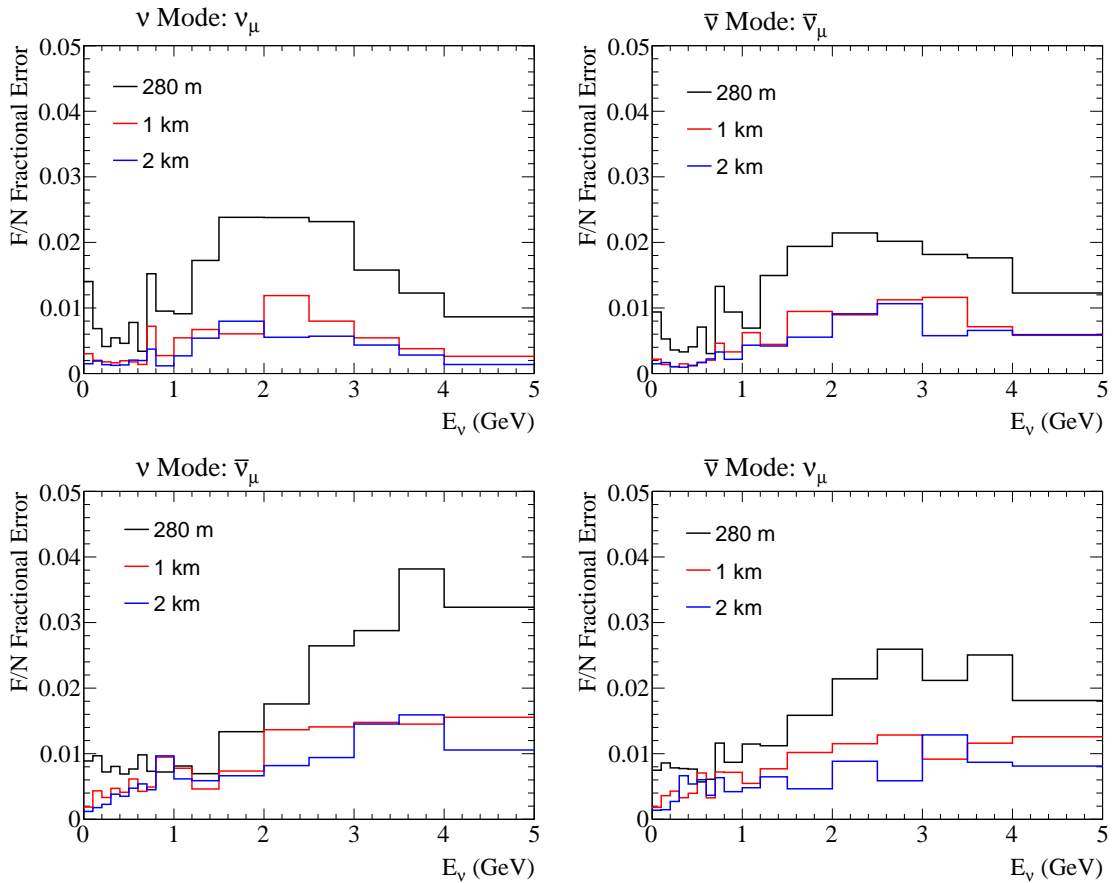


FIG. 15. The uncertainty on the far-to-near flux ratio for near detectors at 280 m, 1 km and 2 km. Left: neutrino enhanced beam. Right: antineutrino enhanced beam. Top: the focused component of the beam. Bottom: the defocused component of the beam.

2. The neutrino beam direction

The previously described uncertainties assume that the near detector is located on the line from the average neutrino production point to Hyper-K. This is expected to be the optimal configuration for uncertainties on the beam direction. If the off-axis near detector only covers a small solid angle, it is only sensitive to changes in the off-axis angle, and cannot distinguish between vertical or horizontal shifts of the neutrino beam direction. For a near and far detector on the same line, the effects of vertical or horizontal shifts are the same and uncertainties on the beam direction cancel in the far-to-near ratio. The T2K ND280 detector is situated on the line to Super-K.

Two sites are being considered for Hyper-K, the Mozumi site near Super-K and the Tochibora site. As illustrated in Fig. 2, the horizontal displacement from the beam direction for these two sites is opposite, hence ND280 is not situated on the line to the Tochibora site. The bias on the far-to-near ratio when the horizontal displacement of the near detector is opposite to the far detector is estimated when the beam is shifted by 0.1 mrad in the horizontal direction, the current uncertainty on the beam direction measurement by the T2K INGRID detector. As Fig 16 shows that the far-to-near ratio can be distorted by 1% for a 0.1 mrad horizontal shift when the near detector and far detector are not on the same line. This may be a significant source of uncertainty for estimation of the flux at Hyper-K and must be considered when designing the near detectors for Hyper-K.

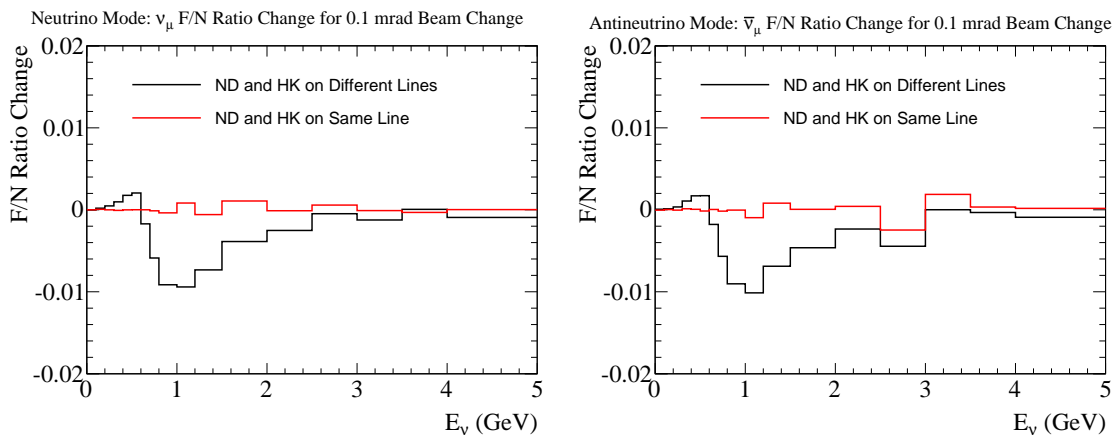


FIG. 16. The change to the far-to-near ratio when the beam is shifted in the horizontal direction by 0.1 mrad toward the far detector. The ratio is unchanged when the near and far detector are in the same direction (red), and changed by up to 1% when the near and far detector are not in the same direction.

IV. NEAR DETECTORS

The accelerator neutrino event rate observed at Hyper-K depends on the oscillation probability, neutrino flux, neutrino interaction cross-section, detection efficiency, and the detector fiducial mass of Hyper-K. To extract estimates of the oscillation parameters from data, one must model the neutrino flux, cross-section and detection efficiency with sufficient precision. In the case of the neutrino cross-section, the model must describe the exclusive differential cross-section that includes the dependence on the incident neutrino energy, E_ν , the kinematics of the outgoing lepton, p_l and θ_l , and the kinematics of final state hadrons and photons. In our case, the neutrino energy is inferred from the lepton kinematics, while the modeling of reconstruction efficiencies depends on the hadronic final state as well.

The neutrino flux and cross-section models can be constrained by data collected at near detectors, situated close enough to the neutrino production point so that oscillation effects are negligible. Our approach to using near detector data will build on the experience of T2K while considering new near detectors that may address important uncertainties in the neutrino flux or cross-section modeling.

The conceptual design of the near detectors is being developed based on the physics sensitivity studies described in Section V. In this section, we present basic considerations on the near detector requirements and conceptual designs. More concrete requirements and detector design will be presented in future. We first discuss the current understanding of neutrino cross section based on the T2K experience and issues relevant for the near detector requirements. Then, the design, performance, and future prospects of T2K near detectors are described as a reference. In order to further reduce the uncertainty and to enhance the physics sensitivity of the project, we have been studying a possibility of building new detectors. As examples of such new detectors, two possible design of new intermediate water Cherenkov detectors are presented.

A. Neutrino cross section uncertainties relevant for near detector requirements

T2K has successfully applied a method of fitting to near detector data with parameterized models of the neutrino flux and interaction cross-sections. The model parameters in the flux and nucleon level cross-section description are constrained by the near detector data so that their contribution to the uncertainty on the Super-K event rate predictions is reduced to only $\sim 3\%$, as discussed in Section IV B 3. However, additional uncertainties on the modeling of nuclear effects

and the modeling of the ν_e interaction cross section relative to the ν_μ cross section contribute an uncertainty of 5-10% on the Super-K event rate predictions. A brief description of these important cross-section model uncertainties is given here.

The use of near detector data is complicated by the fact that the neutrino beam's energy dependence and flavor content at the near and far detectors can be different due to the neutrino oscillations. This complication introduces critical sources of uncertainty for future long baseline experiments measuring CP violation:

- The relative cross-section for ν_μ and ν_e interactions.
- The relationship between the incident neutrino energy and the final state kinematics used to estimate the true neutrino energy. In our case, this is the charged lepton four momentum.
- The difference in the reaction cross-sections on different nuclei in the near and far detectors in the case that those target nuclei are different.

Since the intrinsic ν_e contribution in the beam is $\sim 1\%$, using the near detector data to constrain the ν_e interaction cross-section is challenging. Recent work has shown that theoretical uncertainties on the cross section ratio $\sigma_{\nu_e}/\sigma_{\nu_\mu}$ can be a few percent at the relevant energy and mimic a CP violation effect with opposite sign for neutrinos and antineutrinos [62]. The potential to measure ν_e interactions in the T2K near detectors and new near detectors is discussed in the following sections.

The oscillation probability depends on the neutrino energy, while we estimate the neutrino energy from the observed four momentum of the final state charged lepton. Correctly modeling the relationship between neutrino energy and final state lepton kinematics is essential to correctly applying the oscillation probability, even when there is a constraint on the event rate from near detector data. The signal modes are a charge lepton in the final state, with no detected pion. The main contribution to this topology is charge current quasi-elastic (CCQE) scatters, where the neutrino energy can be estimated from final state lepton momentum and scattering angle. In recent years, much theoretical work has been done to calculate contributions to this topology from non-CCQE processes such as, two body currents or final state interactions that can absorb a pion [63–71]. These nuclear effects often lead to the ejection of multiple nucleons in the final state and are referred to as multinucleon processes here. The additional final state nucleons can carry away energy, leading to kinematics that are different from CCQE scatters. Currently, the

theoretical calculations do not all agree with one another and do not include all processes leading to such invisible energy loss.

Even if models disagree, these effects may be constrained by data from near detectors and dedicated cross-section experiments [72–75]. However, such measurements of the reaction rate or of the nucleon content of the final state can only test one of these calculations within a model, and do not directly probe the relationship of final state kinematics to neutrino energy. Since the multinucleon processes arise from nuclear effects, near detector measurements with the same nuclear target as the far detector are preferred. These may be made with the existing (Section IV B 3) or upgrade (Section IV B 4) of T2K near detectors, or new near detectors (Section IV C). Additionally, the relationship between the incident neutrino energy and final state lepton four momentum can be studied in more detail by using multiple neutrino spectra with different peak energies, as discussed in Section IV C 2.

B. The T2K near detectors

1. The T2K INGRID and ND280 detectors

The INGRID detector [76] consists of 16 iron-scintillator modules configured in a cross pattern centered on the beam axis 280 m downstream from the T2K target, as shown in Fig. 17. The rate of interactions in each module is measured and a profile is constructed to constrain the neutrino beam direction. The ND280 off-axis detector is located 280 m downstream from the T2K target as well, but at an angle of 2.5 degrees away from the beam direction. Fig. 17 shows the components of ND280: the P0D π^0 detector [77], time projection chambers (TPCs) [78], fine grain scintillator bar detectors (FGDs) [79] and surrounding electromagnetic calorimeters (ECALs). The detectors are immersed in a 0.2 T magnetic field and the magnetic yoke is instrumented with plastic scintillator panels for muon range detection [80]. The magnetic field allows for momentum measurement and sign selection of charged particles. The magnetization of ND280 is particularly important for operation in antineutrino mode where the neutrino background is large. In that case, ND280 is able to separate the “right-sign” μ^+ from the “wrong-sign” μ^- . The P0D and FGDs act as the neutrino targets, while the TPCs provide measurements of momentum and ionizing energy loss for particle identification. The P0D and one of the FGDs include passive water layers that allow for neutrino interaction rate measurements on the same target as Super-K. ND280 has been employed to measure the rates of charged current ν_μ and ν_e interactions, as well as NC π^0 interactions.

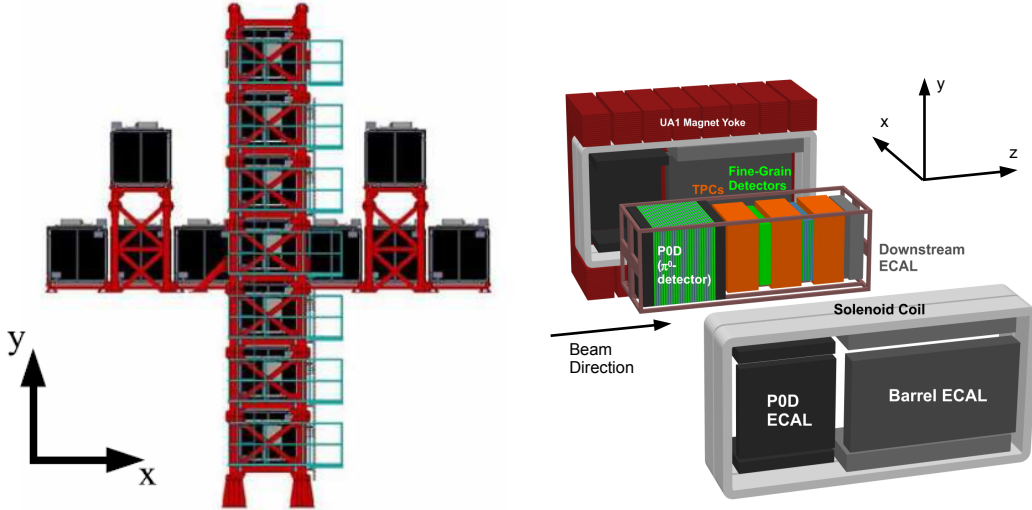


FIG. 17. The INGRID detector modules (left) and the exploded view of the ND280 off-axis detector (right).

2. The INGRID beam direction measurement

The INGRID detector is used to measure the neutrino beam direction. Neutrino interactions originating in each INGRID module are detected and corrections including those for events originating in the surrounding sand and inefficiencies in event pile-up detection, *i.e.* more than one event for beam bunch, are applied. The profiles of event rates across the vertical and horizontal arrays of modules are fit to extract the beam center. Systematic uncertainties on the beam center measurement are 0.094 mrad and 0.104 mrad for the horizontal and vertical respectively. As discussed in Section III C 2, a precise knowledge of the beam direction is important if the off-axis near detector and far detector are not situated along the same direction. The 0.1 mrad systematic error from INGRID is sufficient to control the flux extrapolation uncertainty due to the uncertainty on the beam direction to $< 1\%$ in that scenario, under the assumption that the beam direction constraint from INGRID can be extrapolated to 2.5 degrees off-axis.

3. ND280 measurements

The ND280 detector is used to measure charge current (CC) interaction rates binned by lepton kinematics and hadronic final states, as well as neutral current (NC) interactions with detected π^0 , π^\pm or protons in the final state. These measurements are used to constrain the neutrino flux and cross-section models, including the ν_e contamination of the beam.

TABLE XII. The measured and predicted number of events in the ND280 ν_μ CC enhanced samples.

	CC0 π	CC1 π	CC Other	CC Inclusive
Data	17369	4047	4173	25589
Model before data constraint	19980	5037	4729	29746
Model after data constraint	17352	4110	4119	25581

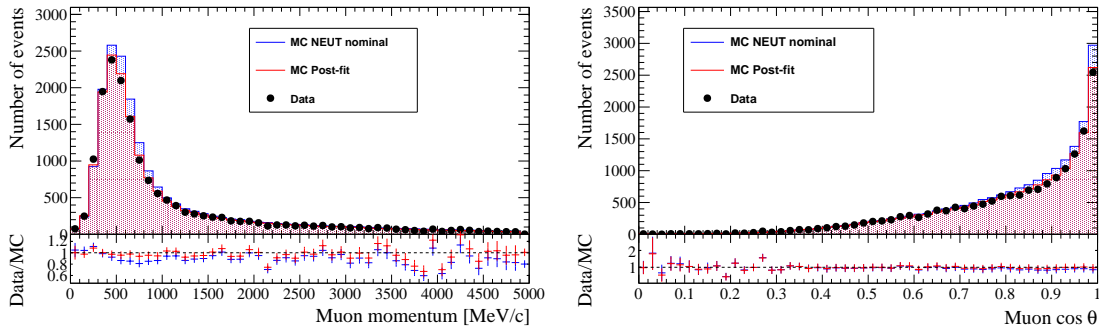


FIG. 18. The momentum (left) and angle (right) distributions for the CC0 π data set. The blue histograms are the predicted distribution before constraining the flux and cross-section models with a fit to the data. The red histograms are the predicted distributions after the constrain from the data.

a. ND280 ν_μ CC measurement The ν_μ charged current interactions in ND280 are used to constrain the neutrino energy spectrum and cross-section model parameters. CC events are selected with a vertex in the most upstream FGD (FGD1) with a track passing through the second TPC and having an energy loss consistent with a muon. The selected CC candidate events are divided into several samples to help constraining the cross-sections: CC-0 π , with no identified pions; CC-1 π^+ , with exactly one π^+ and no π^- or π^0 ; and CC-other, with all the other CC events. The current analysis uses interactions in FGD1, which consists only of plastic scintillator targets.

The numbers of selected events for 5.9×10^{20} protons on target are shown in Table XII. These data are fit while allowing the flux and cross-section model parameters to vary, and the improved agreement in the modeled event rates and muon kinematic distributions can be seen in Table XII and Fig. 18.

The constrained flux and cross-section parameters related to the nucleon level cross-section are used to predict the ν_μ and ν_e interaction rates at Super-K. The uncertainties on these parameters are reduced by the fit to ND280 data, hence reducing the uncertainties on the predicted Super-K event rates, as shown in Table XIII. The overall event rate uncertainties for the ν_μ and ν_e candidate

TABLE XIII. The uncertainties on the SK ν_μ and ν_e candidate rate predictions.

Source	Before ND280 Data Constraint		After ND280 Data Constraint	
	ν_μ Candidates	ν_e Candidates	ν_μ Candidates	ν_e Candidates
Constrained Flux & Cross-section Param.	21.6%	26.0%	2.7%	2.9%
Unconstrained Cross-Section Param.	5.9%	7.6%	4.9%	7.6%
Super-K Modeling Uncertainties	6.3%	3.5%	5.6%	3.5%
Total Error	23.4%	27.5%	8.1%	8.9%

predictions are reduced from 23.4% and 27.5% to 8.1% and 8.9% respectively.

The “Unconstrained Cross-section Param.” uncertainty in Table XIII is dominated by uncertainties in the modeling of the target oxygen nucleus. Thus far, the ND280 analyses used in the oscillation measurement have only used interactions in FGD1, which is composed entirely CH scintillator bars with no oxygen targets. The downstream FGD2 contains layers of water interspersed within its scintillator layers. A simultaneous fit of the interactions in both FGDs can provide a constraint on nuclear effects in oxygen, and may potentially reduce the corresponding nuclear model uncertainties. The ultimate event samples in both FGDs are shown in Table XIV. The statistical precision of a subtraction of interactions on scintillator from interactions on water is better than 1%, which is more precise than current detector systematic uncertainties ($\sim 3\%$). Implementing the FGD2 data to reduce the cross-section modeling uncertainties is a high priority for T2K.

Additionally, the P0D is capable of operating with and without water targets dispersed throughout its active volume, measuring the event rates separately in these two configurations. A CC ν_μ event selection with the P0D and downstream TPC can produce samples of forward muons produced in the P0D water layers. The expected P0D event rates are given in Table XIV.

As discussed in the Section IV, there are large uncertainties in the theoretical modeling of interactions that involve the ejection of no pions and multiple nucleons. T2K has studied the potential biases from the mismodeling of these nuclear effects on the measurements of θ_{23} and Δm_{32}^2 in fits to ν_μ candidates at SK [81]. Toy data for both ND280 and SK are generated using NEUT with additional two body current interactions based on the model of Nieves *et al.* [71]. In addition to the Nieves model a second ad-hoc simulation of two-body currents was studied. This ad-hoc model was chosen to cover the range of two-body current calculations in the literature. Fig. 19 illustrates the energy reconstruction bias from two-body currents in the calculation of Nieves *et al.*

TABLE XIV. The number of selected CC-Inclusive events in FGD1, FGD2, and the P0D are given for the ultimate expected T2K POT assuming 50% ν -mode horn operation and 50% $\bar{\nu}$ -mode for. The subset of events that are right-sign interactions (i.e. ν -interactions in ν -mode and $\bar{\nu}$ interactions in $\bar{\nu}$ -mode) on water are shown separately.

		Total	Right-Sign Event
Event Sample		Event Rate	Rate on Water
ν -mode	FGD1	169,000	–
	FGD2	166,000	84,000
	P0D Water Out	144,000	–
	P0D Water In	10,000	66,000
$\bar{\nu}$ -mode	FGD1	57,000	–
	FGD2	56,000	28,000
	P0D Water Out	63,000	–
	P0D Water In	93,000	30,000

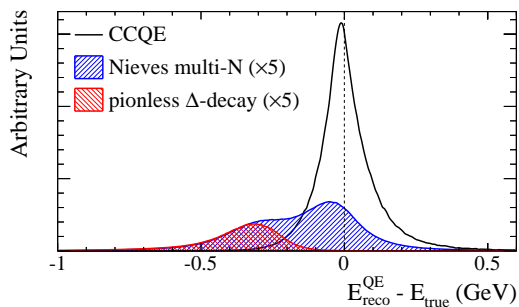


FIG. 19. The difference between the energy reconstructed assuming quasi-elastic kinematics and the true energy for events with no pions in the final state. Black are the NEUT simulation of CCQE events and red are the NEUT simulation of resonant production where the Δ is absorbed. The blue is the from the two-body current calculation of Nieves *et al.* [71].

Both the ND280 and SK toy data are fit assuming the NEUT model, as they are fit in the T2K oscillation analyses, and the biases on θ_{23} and Δm_{32}^2 are evaluated when there are additional two-body current contributions in the toy data. The average and RMS of the oscillation parameter biases for many toy experiments are shown in Table. XV. The average bias can be as large as 2.9% on θ_{23} while there is an additional variation of the bias by as much as 3.6%, for individual toy experiments. This study indicates that the modeling of two-body currents and other nuclear effects can be a dominant systematic effect, even when ND280 data are used to constrain the neutrino

TABLE XV. The oscillation parameter average bias and RMS bias of toy experiments with two body current models.

Model	θ_{23}		Δm_{32}^2	
	Bias	Mean Bias RMS	Bias	Mean Bias RMS
Nieves <i>et al.</i> [71]	0.3%	3.6%	-0.2%	0.6%
Ad-hoc Model	-2.9%	3.2%	0.5%	0.6%

interaction model. Addressing uncertainties in the modeling of two-body currents with additional data from the hadronic final states or novel approaches using the final state lepton kinematics will be necessary to control these uncertainties for future experiments.

b. ND280 cross checks of CC ν_e and NC π^0 rates Currently, T2K also uses ND280 to make cross-checks on the rate of ν_e CC interactions [82] and NC π^0 interactions, both important backgrounds for the ν_e appearance measurement at Super-K.

The ND280 ν_e CC candidates are selected in a similar manner to the ν_μ candidates with the following changes: candidates from interactions in the downstream FGD2 are included, the ionizing energy loss must be consistent with an electron, ECAL showers are used in the particle identification when present, a veto on e^+e^- pairs is applied, and a veto on events with reconstructed upstream objects is applied to reduce the γ background. The data are broken into CCQE-like and CCnonQE-like sub-samples, shown in Fig. 20. A fit of the flux and cross-section models to the data provides a ratio of measured ν_e CC interactions to the model prediction, 1.01 ± 0.10 (syst+stat.). The most relevant data for the T2K oscillation measurements are interactions of ν_e with $E_\nu < 1.5$ GeV. These tend to populate the low momentum region where there is a large background from converting photons. Reducing this background to improve the constraint for the T2K oscillation analysis is a challenge and high priority for ND280.

ND280 measures the rate of NC π^0 with the P0D detector from a data set corresponding to 8.55×10^{19} POT. When normalized to the ND280 CC ν_μ data, the measured a ratio of the data rate over the model prediction is 0.81 ± 0.15 (stat.) ± 0.14 (syst.). This selection of π^0 candidates is limited to the forward region, $\cos(\theta_\pi) > 0.6$, whereas Super-K can detector photons from π^0 decays with 4π coverage. The current measurement does not separate events on water or other materials in the P0D. Future analysis will attempt to address these limitations in the current measurement.

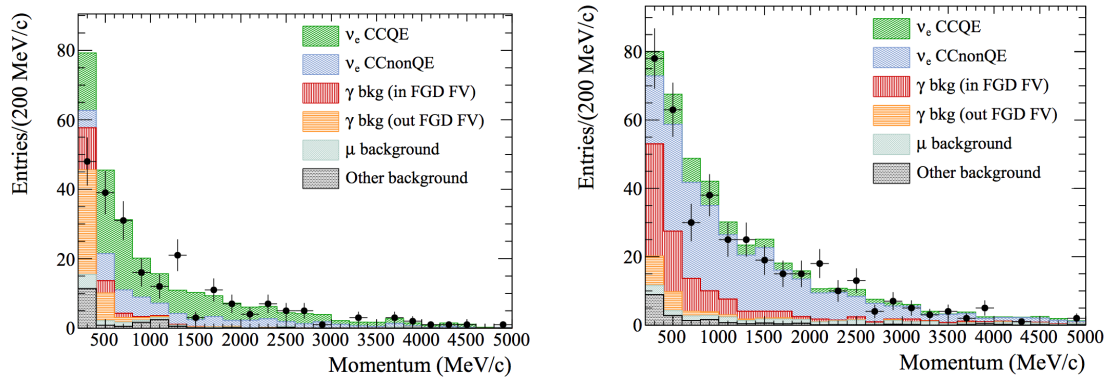


FIG. 20. The ND280 CC ν_e candidates in the CCQE-like (left) and CCnonQE-like (right) sub-samples. The predicted rates are shown in the stacked color histograms.

4. Potential ND280 upgrades

The T2K collaboration is in the process of discussing various upgrade possibilities at the ND280 site. These include the deployment of heavy water (D_2O) within the passive water targets in FGD2 that would allow the extraction of neutrino interaction properties on the quasi-free neutron in deuterium via a subtraction with data taken with light water H_2O . The use of a water-based liquid scintillator (WbLS) developed at BNL is being explored in the context of a tracking detector with comparable or finer granularity than the FGD to allow the detailed reconstruction of hadronic system emerging from the neutrino interactions or a larger detector with coarser segmentation that would allow high statistics studies. Either would significantly enhance the study of neutrino interactions on water by reducing the reliance on subtraction and enhancing the reconstruction capabilities relative to the currently deployed passive targets. Finally, a high pressure TPC that can contain various noble gases (He, Ne, Ar) to serve both as the target and tracking medium is being studied. Such a detector would allow the ultimate resolution of the particles emitted from the target nucleus while allowing a study of the A -dependence of the cross-sections and final state interactions to rigorously test models employed in neutrino event generators.

While the above options would be deployed within the UA1 magnet, another proposal would place a scintillating tracking detector outside of the magnet on the B2 floor of the NU1 building surrounded by range detectors to measure the muon momentum over a large range of angles. The inner tracking detector would allow passive water and plastic targets to be deployed in order to measure water and CH cross-sections.

C. Intermediate water Cherenkov detectors

Since many of the uncertainties on the modeling of neutrino interactions arise from uncertainties on nuclear effects, the ideal near detector should include the same nuclear targets as the far detector. The ND280 POD and FGD detectors include passive water layers, however extracting water only cross sections requires complicated analyses that subtract out the interactions on other materials in the detectors. An alternative approach is to build a water Cherenkov (WC) near detector to measure the cross section on H_2O directly and with no need for a subtraction analysis. This approach was taken by K2K [30] and was proposed for T2K [83]. The MiniBooNE experiment has also employed a mineral oil Cherenkov detector at a short baseline to great success [84]. A WC near detector design is largely guided by two requirements:

1. The detector should be large enough to contain muons up to the momentum of interest for measurements at the far detector.
2. The detector should be far enough from the neutrino production point so that there is minimal pile-up of interactions in the same beam timing bunch.

These requirements lead to designs for kiloton size detectors located at intermediate distances, 1-2 km from the target, for the J-PARC neutrino beam.

The main disadvantage of the WC detector is the inability to separate positively and negatively charged leptons, and hence antineutrino and neutrino interactions. This ability is especially important for a CP violation measurement where the wrong sign contribution to the neutrino flux should be well understood. Hence, the WC detector will most likely be used in conjunction with a magnetized tracking detector such as ND280. Recent developments in the addition of Gadolinium (Gd) and Water-based Liquid Scintillator (WbLS) compounds to water do raise the possibility to separate neutrino and antineutrino interactions by detecting the presence of neutrons or protons in the final state.

Two conceptual designs for possible intermediate WC detectors have been studied and are described in this section. The Tokai Intermediate Tank for Unoscillated Spectrum (TITUS) is a 2 kiloton WC detector located about 2 km from the target at the same off-axis angle as the far detector. At this baseline the detector sees fluxes for the neutral current and ν_e backgrounds that are nearly identical to the Hyper-K fluxes. The detector geometry and the presence of a muon range detector are optimized to detect the high momentum tail of the muon spectrum. The use of Gd in TITUS to separate neutrino and antineutrino interactions is being studied. The ν PRISM

detector is located 1 km from the target and is 50 m tall, covering a range of off-axis angles from 1-4 degrees. The ν PRISM detector sees a range of neutrino spectra, peaked at energies from 0.4 to 1.0 GeV. The purpose of nuPRISM is to use these spectra to better probe the relationship between the incident neutrino energy and final state lepton kinematics, a part of the interaction model with larger uncertainties arising from nuclear effects.

1. The TITUS water Cherenkov detector

As discussed in the previous text, the challenges in the use of ND280 data include the measurement of a different flux than at SK, the limited phase space coverage, and the implementation of analyses to extract cross-sections on water. These limitations can be addressed with a complementary water Cherenkov detector strategically located at an intermediate distance of about 2 km from the neutrino production point.

At this distance, the TITUS detector sees almost the same spectrum as at Hyper-K. The maximum difference in shape is $\sim 5\%$ at the peak energy instead of almost 20% with ND280, see Fig. 21 (left) for the ratio.

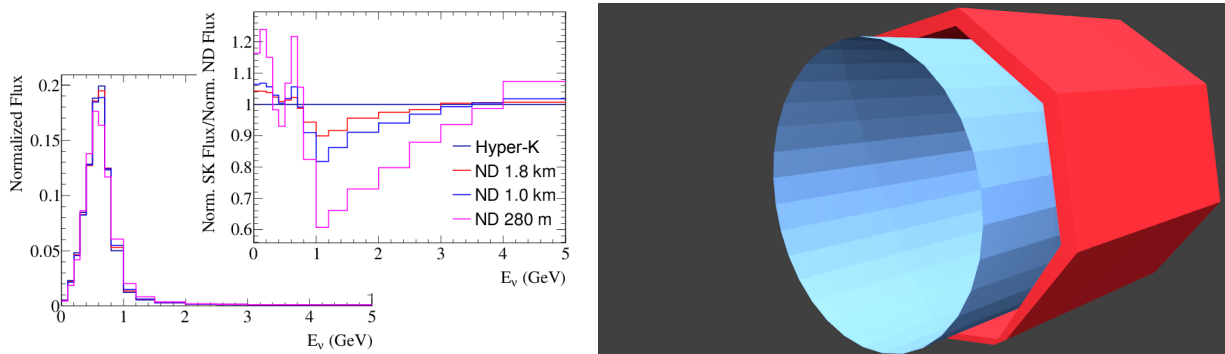


FIG. 21. Left: neutrino energy spectrum at different baselines, and corresponding far-to-near ratio. Right: Detector design, consisting of a WC Gd-doped tank (blue) surrounded by a MRD or MIND detector (red).

The TITUS detector consists of a 2 kton Gd-doped WC tank (about 5.5 m radius for about 22 m length) surrounded by a Muon Range Detector (MRD) or a Magnetized Iron Neutrino Detector (MIND) covering 3/4 of the length of the sides and the downstream of the detector (see Fig. 21). Optimization of the dimensions and shape of the tank and the MRD or MIND is in progress. The current detector size was chosen using two main criteria: muon containment and pile-up.

The photosensors planned to be used are both LAPPDs and HPDs. The LAPPDs will provide

TABLE XVI. Expected true neutrino interaction event rates at TITUS for fiducial volumes (FV) of 2 kton and 1.17 kton for the full proposed beam run in neutrino- and anti-neutrino-enhanced modes (3.9×10^{21} and 11.7×10^{21} POT, respectively). Coherent pion production is in the “Other” category; resonant pion production is in 1π . The category labeled MEC are multinucleon ejection events modeled based on the calculations of Nieves *et. al.* [71]

Interaction:	ν_μ CC (10^4)				$\bar{\nu}_\mu$ CC (10^4)			ν_e CC (10^4)		$\bar{\nu}_e$ CC (10^4)		NC (10^4)	
	QE	MEC	1π	Other	QE	MEC	Other	QE	Other	QE	Other	π^0	Other
+320kA (FV = 2 kton)	428	72.5	236	143	8.37	2.30	12.4	5.26	13.8	0.411	1.07	55.8	249
+320kA (FV = 1.17 kton)	240	40.6	132	79.8	4.68	1.29	6.95	2.95	7.75	0.230	5.97	31.3	139
-320kA (FV = 2 kton)	93.0	20.5	99.9	122	276	62.8	184	3.41	13.1	3.95	7.15	59.8	307
-320kA (FV = 1.17 kton)	52.0	11.5	55.9	68.5	154	35.1	103	1.91	7.35	2.21	4.00	33.5	172

excellent time and spatial resolution that will greatly aid the reconstruction, and will provide very good identification of the NC π^0 events that are a major background for electron neutrino appearance at Hyper-K.

We seek to take advantage of the ANNIE experiment [85], should it be funded and running in the next years, to provide an additional environment for testing. The ANNIE experiment has a similar configuration, but smaller size, than TITUS.

The number of events observed by the detector at 2 km are shown in Table XVI.

Adding Gd to the water provides TITUS with excellent neutron tagging capabilities. With a 0.1% concentration, $\sim 90\%$ of neutrons will capture on Gd, producing a 8 MeV gamma cascade of typically 2-3 gammas from neutrino capture, resulting in sufficient optical light to be detected in the volume. Tagging events by the presence and number of final-state neutrons provides a unique capability to discriminate between different species of neutrino interactions (e.g. CCQE vs MEC separation, NC versus CC separation, $\bar{\nu}/\nu$, ν_e/ν_μ). For instance, Fig. 22 (left) shows the current nucleon multiplicity prediction after FSI, assuming that that the n - p pair is 80% and dominant, where the n - n and p - p pairs are 10% each, as nuclear theorists speculate [86] and partially supported by electron scattering data [87]. The error on the FSI neutrons is on the order of 3%(33%) for CCQE(MEC) interactions on water. As figure shows, different interaction types have different nucleon multiplicities and counting nucleons gives an additional handle to study them. This would improve our knowledge on neutrino cross-sections, and eventually reduce the error on the far detector measurements coming from neutrino cross-sections.

The thermal neutrons, in particular the spallation neutrons from cosmic rays, are potential

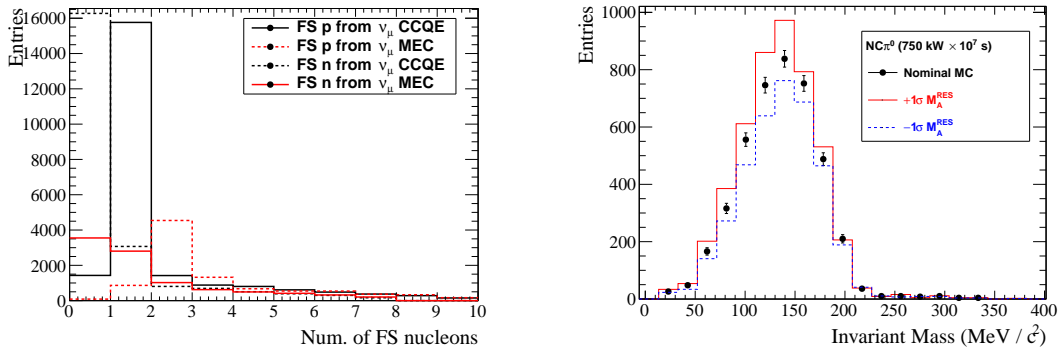


FIG. 22. Left: nucleon multiplicity for interaction final states. Right: reconstructed π^0 mass from NC π^0 events.

backgrounds that can change the neutron counting scheme. From an initial investigation based on the Super-K analysis, they can be strongly suppressed by tagging the parent cosmic rays. The neutron background coming from the beam totals about one per particle/bunch (including also the interactions with the surrounding rock), that can be further reduced by a selection.

The gadolinium-doped design of TITUS makes possible the characterization of ν versus $\bar{\nu}$, significantly reducing the error on the $\bar{\nu}/\nu$ ratio. The anti-neutrino interactions have higher neutron multiplicities than neutrino interactions.

The detector will allow NC π^0 events to be clearly identified. Within one year of running the uncertainty on the NC π^0 rate will be known better than the current error on the axial mass, see Fig. 22 (right).

The observed ν_e/ν_μ candidate ratio in TITUS is used to estimate the ν_e beam contamination and to constrain uncertainties on the relative reaction cross-sections of ν_e and ν_μ . Using a selection similar to the current T2K selection at SK for ν_e and ν_μ shows that a statistical precision of 1-2% on the measurement of the ν_e rate can be achieved. The complete uncertainty on the interaction rate will depend on the uncertainties in the muon and neutral current backgrounds. The uncertainty on the reaction cross-section measurement will also depend on the flux uncertainty that can be achieved.

Finally, there are a range of further important studies that the detector will be able to address. In particular, the measurement of the neutron rate, that is a crucial background in the proton decay search; supernova neutrinos, TITUS can be included in the SNEWS (SuperNova Early Warning system); reactor neutrinos, under the assumption of a reactor operating close-by, this detector would be able to measure the reactor rate.

2. The ν PRISM detector

The problem of determining the relationship between neutrino energy and lepton kinematics in $CC0\pi$ interactions could be easily solved if mono-energetic beams of neutrinos could be produced at $\mathcal{O}(1 \text{ GeV})$. While mono-energetic beams cannot be produced, beams of varying peak energy can be produced by changing the off-axis angle of the beam. Fig. 24 shows how the neutrino flux varies from an off-axis angle of 1° to 4° . The ν PRISM detector, as illustrated in Fig. 23, would consist of a vertical column water cherenkov detector located $\sim 1 \text{ km}$ from the neutrino production point, and extending over a $3\text{-}4^\circ$ range of off-axis angles. Using ν PRISM and the neutrino flux prediction, it is possible to detect interactions from a variety of neutrino spectra by identifying the off-axis angles using the location of the interaction vertices in the detector. Hence the dependence of final state lepton kinematics on neutrino energy can be studied with a single detector and a single neutrino beam.

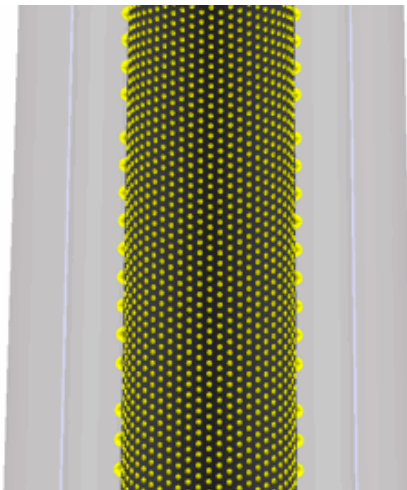


FIG. 23. An illustration of a ν PRISM detector segment showing the vertical cylinder geometry with inward facing photo-multiplier tubes viewing an inner detector and outward facing photo-multiplier tubes viewing an outer detector. At a baseline of 1 km , the ν PRISM cylinder would be 50 m tall.

The expected detected event rates for single-ring lepton candidates in ν PRISM with neutrino mode and antineutrino mode beams are shown in Table XVII. Pure, high statistics samples of charged current ν_μ candidates can be detected. When operating with the antineutrino enhanced beam, the purity is reduced due to the neutrino background, however the properties of this background can be well constrained by the neutrino flux prediction and ν PRISM measurements made with the neutrino enhanced beam.

TABLE XVII. The event rates and purities for single muon-like ring and single electron-like ring selections for 3.9×10^{21} (11.7×10^{21}) POT in the ν PRISM detector with neutrino (antineutrino) mode.

Off-axis Angle ($^\circ$)	1 Ring μ		1 Ring e	
	Candidates	CC $\nu_\mu(\bar{\nu}_\mu)$ Purity	Candidates	CC $\nu_e(\bar{\nu}_e)$ Purity
1.0-2.0	$3.42 \times 10^6(3.06 \times 10^6)$	97.5%(84.7%)	$2.56 \times 10^4(2.95 \times 10^4)$	45.8%(27.1%)
2.0-3.0	$1.76 \times 10^6(1.65 \times 10^6)$	97.7%(81.8%)	$1.36 \times 10^4(1.66 \times 10^4)$	67.2%(38.0%)
3.0-4.0	$7.85 \times 10^5(8.02 \times 10^5)$	97.2%(76.2%)	$7.91 \times 10^3(1.09 \times 10^4)$	74.9%(40.1%)

The ν PRISM detector is also well optimized to study the ν_e contamination in the beam from muon and kaon decays. The ν PRISM measurement of ν_e candidates at 2.5° off-axis angle can be used to predict the expected ν_e background rate at Hyper-K. The ν_e candidates in ν PRISM can also be used to make measurements of the ν_e cross-section at $\mathcal{O}(1 \text{ GeV})$. Given recent improvements to the SK reconstruction that reduce the misidentification of muons or π^0 s as electrons, it is possible to select ν_e candidate samples in ν PRISM with $> 70\%$ purity of ν_e charged current interactions. Even higher purities may be achieved by optimizing the granularity of the PMTs used in ν PRISM and optimizing the event reconstruction and selection. As indicated in Table XVII, the highest purity can be achieved at larger off-axis angles, where the background of NC π^0 reactions is reduced due to the decrease in the high energy ν_μ flux. With high purity samples of $1 \times 10^3 - 1 \times 10^4$ events, ν PRISM has the potential to measure the ν_e interaction cross-section relative to the ν_μ interaction cross-section to better than 10% precision, depending on the flux and reconstruction uncertainties that can be achieved.

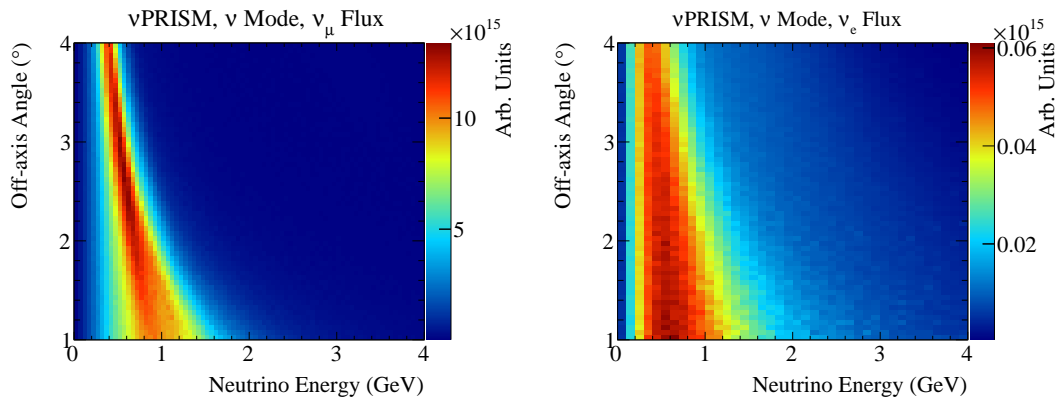


FIG. 24. The predicted ν_μ (left) and ν_e (right) flux for the neutrino enhanced beam as a function of the off-axis angle at the ν PRISM detector.

V. PHYSICS SENSITIVITIES

A. Overview

A comparison of muon-type to electron-type transition probabilities between neutrinos and anti-neutrinos is one of the most promising methods to observe the lepton CP asymmetry. Recent observation of a nonzero, rather large value of θ_{13} [10, 33–35] makes this exciting possibility more realistic.

Figure 25 shows the $\nu_\mu \rightarrow \nu_e$ and $\bar{\nu}_\mu \rightarrow \bar{\nu}_e$ oscillation probabilities as a function of the true neutrino energy for a baseline of 295 km. The cases for $\delta_{CP} = 0, \frac{1}{2}\pi, \pi,$ and $-\frac{1}{2}\pi$, are overlaid. Also shown are the case of normal mass hierarchy ($\Delta m_{32}^2 > 0$) with solid lines and inverted mass hierarchy ($\Delta m_{32}^2 < 0$) with dashed lines. The oscillation probabilities depend on the value of δ_{CP} , and by comparing the neutrinos and anti-neutrinos, one can see the effect of CP violation. There are sets of different mass hierarchy and values of δ_{CP} which give similar oscillation probabilities. This is known as the degeneracy due to unknown mass hierarchy and may introduce an ambiguity if we do not know the true mass hierarchy.

Because there are a number of experiments planned to determine mass hierarchy in near future as shown in Table II, it is expected that the mass hierarchy will be determined by the time of Hyper-K. If not, Hyper-K itself has a sensitivity to the mass hierarchy by the atmospheric neutrino measurements as shown in Table III. Furthermore, a combined analysis of the accelerator and atmospheric neutrino data in Hyper-K will enhance the sensitivity as shown in Sec. V F. Thus,

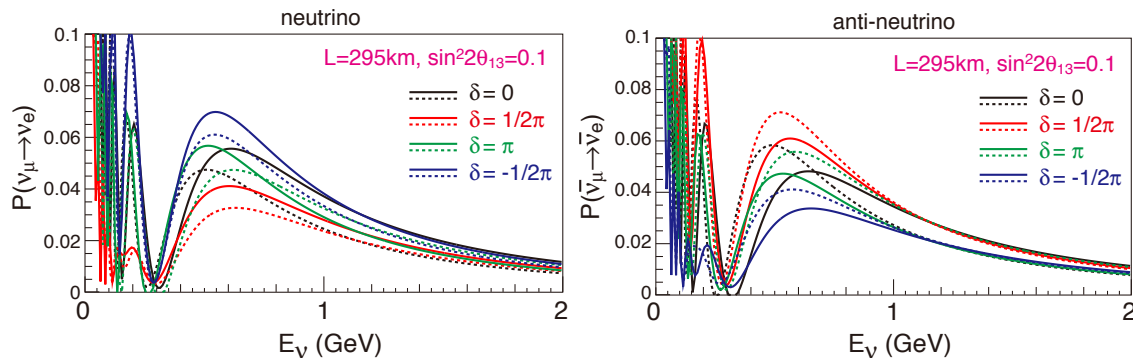


FIG. 25. Oscillation probabilities as a function of the neutrino energy for $\nu_\mu \rightarrow \nu_e$ (left) and $\bar{\nu}_\mu \rightarrow \bar{\nu}_e$ (right) transitions with $L=295$ km and $\sin^2 2\theta_{13} = 0.1$. Black, red, green, and blue lines correspond to $\delta_{CP} = 0, \frac{1}{2}\pi, \pi,$ and $-\frac{1}{2}\pi$, respectively. Solid (dashed) line represents the case for a normal (inverted) mass hierarchy.

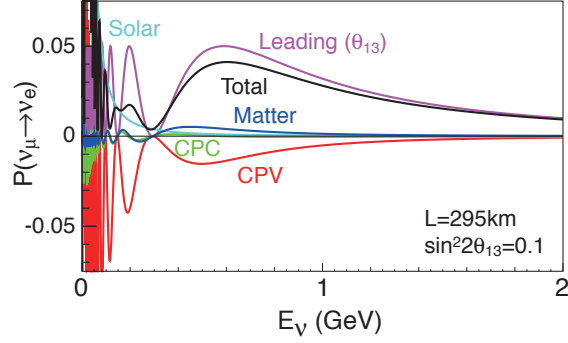


FIG. 26. Oscillation probability of $\nu_\mu \rightarrow \nu_e$ as a function of the neutrino energy with a baseline of 295 km. $\sin^2 2\theta_{13} = 0.1$, $\delta_{CP} = \frac{1}{2}\pi$ and normal hierarchy is assumed. Contribution from each term of the oscillation probability formula is shown separately.

the mass hierarchy is assumed to be known in this analysis, unless otherwise stated.

Figure 26 shows the contribution from each term of the $\nu_\mu \rightarrow \nu_e$ oscillation probability formula, Eq.(4). For $\sin^2 2\theta_{13} = 0.1$, $\sin^2 2\theta_{23} = 1.0$, and $\delta_{CP} = \pi/2$ with normal mass hierarchy, the contribution from the leading term, the CP violating ($\sin \delta_{CP}$) term, and the matter term to the $\nu_\mu \rightarrow \nu_e$ oscillation probability at 0.6 GeV neutrino energy are 0.05, -0.014 , and 0.004, respectively. Due to the relatively short baseline and thus lower neutrino energy at the oscillation maximum, the contribution of the matter effect is smaller for the J-PARC to Hyper-Kamiokande experiment compared to other proposed experiments like LBNE in the United States [88].

In the previous study performed in 2011 [1], the sensitivity was evaluated for a range of θ_{13} values because the exact value of θ_{13} was not known at that time, although T2K collaboration had already reported an indication of electron neutrino appearance [10]. Now that the value of θ_{13} is known rather precisely with reactor experiments [33–35, 89, 90], the sensitivity has been revised with the latest knowledge of the oscillation parameters. In addition, the analysis method is updated using a framework developed for the sensitivity study by T2K reported in [40]. A binned likelihood analysis based on the reconstructed neutrino energy distribution is performed using both ν_e ($\bar{\nu}_e$) appearance and ν_μ ($\bar{\nu}_\mu$) disappearance samples simultaneously. In addition to $\sin^2 2\theta_{13}$ and δ_{CP} , other parameters that were fixed in the previous study, $\sin^2 \theta_{23}$ and Δm_{32}^2 , are also included in the fit. Table XVIII shows the nominal oscillation parameters used in the study presented in this document, and the treatment during the fitting. Systematic uncertainties are estimated based on the experience and prospects of the T2K experiment.

The integrated beam power of $7.5 \text{ MW} \times 10^7 \text{ sec}$ is assumed in this study. It corresponds to 1.56×10^{22} protons on target with 30 GeV J-PARC beam. The ratio of neutrino and anti-neutrino

running time is assumed to be 1:3 so that the expected number of events are approximately the same for neutrino and anti-neutrino modes.

TABLE XVIII. Oscillation parameters used for the sensitivity analysis and treatment in the fitting. The *nominal* values are used for figures and numbers in this section, unless otherwise stated.

Parameter	$\sin^2 2\theta_{13}$	δ_{CP}	$\sin^2 \theta_{23}$	Δm_{32}^2	mass hierarchy	$\sin^2 2\theta_{12}$	Δm_{12}^2
Nominal	0.10	0	0.50	$2.4 \times 10^{-3} \text{ eV}^2$	Normal or Inverted	0.8704	$7.6 \times 10^{-5} \text{ eV}^2$
Treatment	Fitted	Fitted	Fitted	Fitted	Fixed	Fixed	Fixed

B. Expected observables at Hyper-K

The neutrino flux presented in Sec. III C is used as an input to the simulation. Interactions of neutrinos in the Hyper-K detector are simulated with the NEUT program library [91–93], which is used in both Super-K and T2K. The response of the detector is simulated using the Super-K full Monte Carlo simulation based on the GEANT3 package [48]. The simulation is based on the SK-IV configuration with the upgraded electronics and DAQ system. Events are reconstructed with the Super-K reconstruction software. As described in Sec. II F, the performance of Hyper-K detector for neutrinos with J-PARC beam energy is expected to be similar to that of Super-K. Thus, the Super-K full simulation gives a realistic estimate of the Hyper-K performance.

The criteria to select ν_e and ν_μ candidate events are based on those developed for and established with the Super-K and T2K experiments. Fully contained (FC) events with reconstructed vertex inside the fiducial volume (FV) and visible energy (E_{vis}) greater than 30 MeV are selected as FCFV neutrino event candidates. In order to enhance charged current quasielastic (CCQE, $\nu_l + n \rightarrow l^- + p$ or $\bar{\nu}_l + p \rightarrow l^+ + n$) interaction, a single Cherenkov ring is required.

Assuming a CCQE interaction, the neutrino energy (E_ν^{rec}) is reconstructed from the energy of the final state charged lepton (E_ℓ) and the angle between the neutrino beam and the charged lepton directions (θ_ℓ) as

$$E_\nu^{\text{rec}} = \frac{2(m_n - V)E_\ell + m_p^2 - (m_n - V)^2 - m_\ell^2}{2(m_n - V - E_\ell + p_\ell \cos \theta_\ell)}, \quad (9)$$

where m_n, m_p, m_ℓ are the mass of neutron, proton, and charged lepton, respectively, p_ℓ is the charged lepton momentum, and V is the nuclear potential energy (27 MeV).

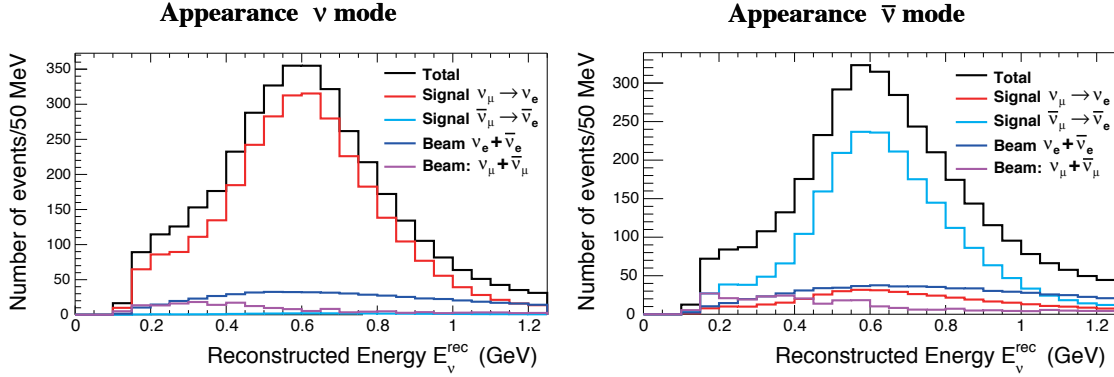

 FIG. 27. Reconstructed neutrino energy distribution of the ν_e candidate events.

 TABLE XIX. The expected number of ν_e candidate events. $\sin^2 2\theta_{13} = 0.1$ and $\delta_{CP} = 0$ are assumed. Background is categorized by the flavor before oscillation.

	signal		BG					total
	$\nu_\mu \rightarrow \nu_e$	$\bar{\nu}_\mu \rightarrow \bar{\nu}_e$	ν_μ CC	$\bar{\nu}_\mu$ CC	ν_e CC	$\bar{\nu}_e$ CC	NC	
ν mode	3016	28	11	0	503	20	172	3750
$\bar{\nu}$ mode	396	2110	4	5	222	396	265	3397

Then, to select $\nu_e/\bar{\nu}_e$ candidate events, following criteria are applied; the reconstructed ring is identified as electron-like (e -like), E_{vis} is greater than 100 MeV, there is no decay electron associated to the event, and E_ν^{rec} is less than 1.25 GeV. Finally, in order to reduce the background from mis-reconstructed π^0 events, additional criteria using a reconstruction algorithm recently developed for T2K (fitQun, see Sec. II F) is applied. With a selection based on the reconstructed π^0 mass and the ratio of the best-fit likelihoods of the π^0 and electron fits as used in T2K [11], the remaining π^0 background is reduced to about 30% compared to the previous study [1].

Figure 27 shows the reconstructed neutrino energy distributions of ν_e events after all the selections. The expected number of ν_e candidate events is shown in Table XIX for each signal and background component. In the neutrino mode, the dominant background component is intrinsic ν_e contamination in the beam. The mis-identified neutral current π^0 production events, which was one of dominant background components in the previous study, are suppressed thanks to the improved π^0 rejection. In the anti-neutrino mode, in addition to $\bar{\nu}_e$ and $\bar{\nu}_\mu$, ν_e and ν_μ components have non-negligible contributions due to larger fluxes and cross-sections compared to their counterparts in the neutrino mode.

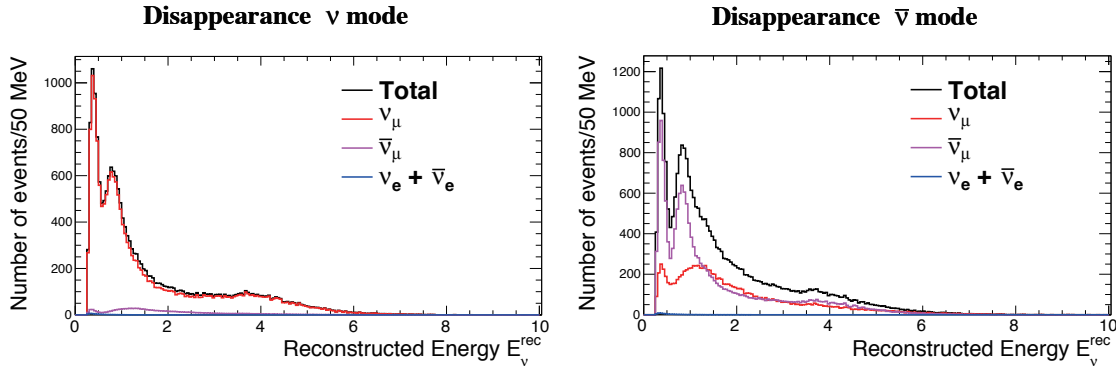


FIG. 28. Reconstructed neutrino energy distribution of the ν_μ candidate events.

TABLE XX. The expected number of ν_μ candidate events.

	ν_μ CC	$\bar{\nu}_\mu$ CC	ν_e CC	$\bar{\nu}_e$ CC	NC	$\nu_\mu \rightarrow \nu_e$	total
ν mode	17225	1088	11	1	999	49	19372
$\bar{\nu}$ mode	10066	15597	7	7	1281	6	26964

For the $\nu_\mu/\bar{\nu}_\mu$ candidate events, following criteria are applied; the reconstructed ring is identified as muon-like (μ -like), the reconstructed muon momentum is greater than 200 MeV/ c , and the number of decay electron associated to the event is 0 or 1.

Figure 28 shows the reconstructed neutrino energy distributions of the selected $\nu_\mu/\bar{\nu}_\mu$ events. Table XX shows the number of ν_μ candidate events for each signal and background component. For the neutrino mode, most of events are due to ν_μ , while in the anti-neutrino mode, contribution from wrong-sign ν_μ component is significant.

The reconstructed neutrino energy distributions of ν_e events for several values of δ_{CP} are shown in the top plots of Fig. 29. The effect of δ_{CP} is clearly seen using the reconstructed neutrino energy. The bottom plots show the difference of reconstructed energy spectrum from $\delta_{CP} = 0^\circ$ for the cases $\delta = 90^\circ, -90^\circ$ and 180° . The error bars correspond to the statistical uncertainty. By using not only the total number of events but also the reconstructed energy distribution, the sensitivity to δ_{CP} can be improved, and one can discriminate all the values of δ_{CP} , including the difference between $\delta_{CP} = 0$ and π . Figure 30 shows the reconstructed neutrino energy distributions of ν_μ sample for several values of δ_{CP} . As expected, difference is very small for ν_μ events.

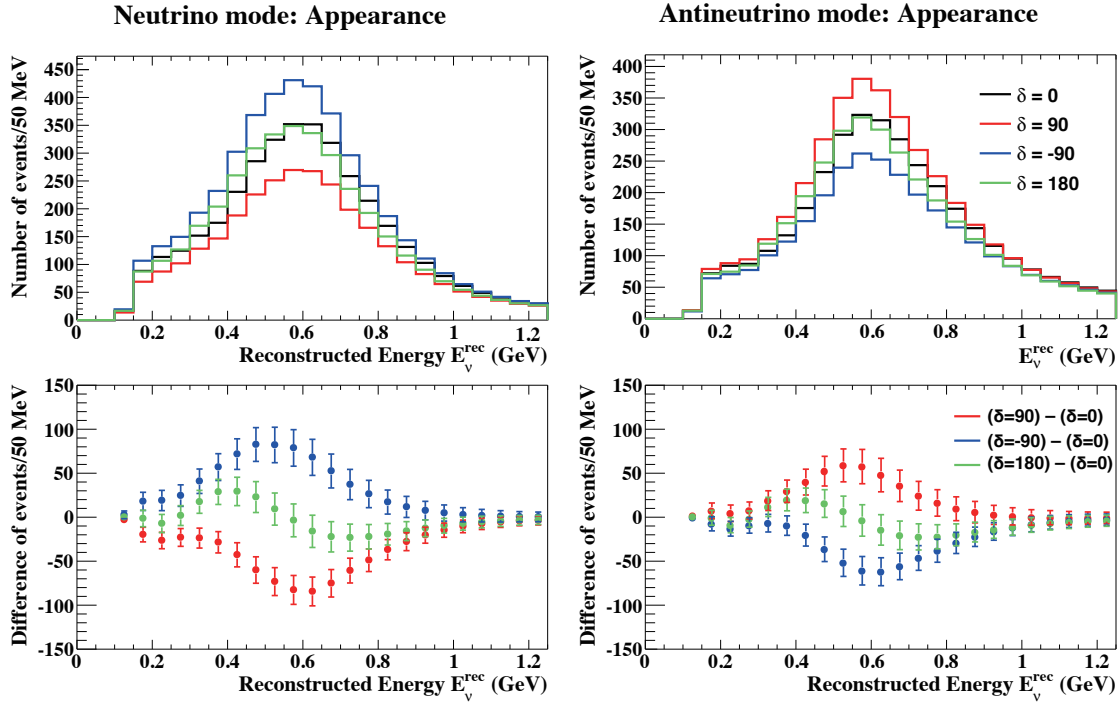


FIG. 29. Top: Reconstructed neutrino energy distribution for several values of δ_{CP} . $\sin^2 2\theta_{13} = 0.1$ and normal hierarchy is assumed. Bottom: Difference of the reconstructed neutrino energy distribution from the case with $\delta_{CP} = 0^\circ$. The error bars represent the statistical uncertainties of each bin.

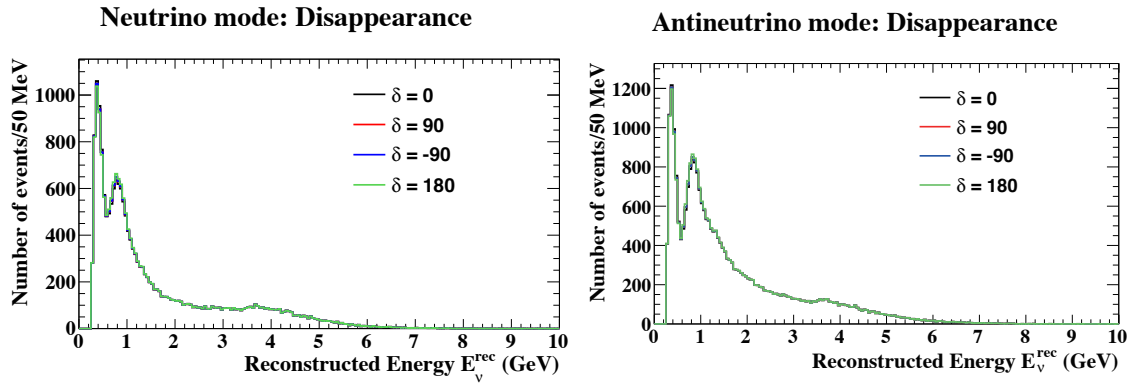


FIG. 30. Reconstructed neutrino energy distribution of ν_μ candidates for several values of δ_{CP} .

C. Analysis method

The sensitivity of a long baseline experiment using Hyper-K and J-PARC neutrino beam is studied using a binned likelihood analysis based on the reconstructed neutrino energy distribution. Both ν_e appearance and ν_μ disappearance samples, in both neutrino and antineutrino running, are simultaneously fitted.

The χ^2 used in this study is defined as

$$\chi^2 = -2 \ln \mathcal{L} + P, \quad (10)$$

where $\ln \mathcal{L}$ is the log likelihood for a Poisson distribution,

$$-2 \ln \mathcal{L} = \sum_k \left\{ -N_k^{\text{test}}(1 + f_i) + N_k^{\text{true}} \ln \left[N_k^{\text{test}}(1 + f_i) \right] \right\}. \quad (11)$$

Here, N_k^{true} (N_k^{test}) is the number of events in k -th reconstructed energy bin for the true (test) oscillation parameters. The index k runs over all reconstructed energy bins for muon and electron neutrino samples and for neutrino and anti-neutrino mode running. The binning of systematic parameter f_i is coarser than the reconstructed energy bins, which are grouped based on the behavior against the systematics uncertainty, with variable widths. For anti-neutrino mode samples, an additional overall normalization parameter with 6% prior uncertainty is introduced to account for possible uncertainty in the anti-neutrino interaction, which is less known experimentally in this energy region. A normalization weight $(1 + f_{\text{norm}}^{\bar{\nu}})$ is multiplied to N_k^{test} in the anti-neutrino mode samples.

The penalty term P in Eq. 10 constrains the systematic parameters f_i with the normalized covariance matrix C ,

$$P = \sum_{i,j} f_i (C^{-1})_{i,j} f_j. \quad (12)$$

The size of systematic uncertainty is evaluated based on the experience and prospects of the T2K experiment, as it provides the most realistic estimate as the baseline. We estimate the systematic uncertainties assuming the T2K neutrino beamline and near detectors, taking into account improvement expected with future T2K running and analysis improvement. For Hyper-K, further reduction of systematic uncertainties will be possible with upgrade of beamline and near detectors, improvement of detector calibration and analysis techniques, and improved understanding of neutrino interaction with more measurements. In particular, as described in Sec. IV, studies of near detectors are ongoing with a goal of further reducing systematic uncertainties. The sensitivity update is expected in near future as the near detector design studies advance.

There are three main categories of systematic uncertainties. We assume improvement from the current T2K uncertainties for each category as follows.

i) Flux and cross section uncertainties constrained by the fit to near detector data:

They are limited by the systematics of near detectors. The understanding of the detector

will improve in future, but this category of uncertainties are conservatively assumed to stay at the same level as currently estimated.

ii) Cross section uncertainties that are not constrained by the fit to near detector data:

Errors in this category will be reduced as more categories of samples are added to the near detector data fit, which constrains the cross section models. We assume the uncertainties arising from different target nucleus between the near and the far detectors will become negligible by including the measurement with the water target in the near detector.

iii) Uncertainties on the far detector efficiency and reconstruction modeling:

Because most of them are estimated by using atmospheric neutrinos as a control sample, errors in this category are expected to decrease with more than an order of magnitude larger statistics available with Hyper-K than currently used for T2K. Uncertainties arising from the energy scale and the final state interaction are kept the same because they are not estimated by the atmospheric neutrino sample.

The flux and cross section uncertainties are assumed to be uncorrelated between the neutrino and anti-neutrino running, except for the uncertainty of ν_e/ν_μ cross section ratio which is treated to be anti-correlated considering the theoretical uncertainties studied in [62]. Because some of uncertainties, such as those from the cross section modeling or near detector systematics, are expected to be correlated and give more constraint, this is a conservative assumption. The far detector uncertainty is treated to be fully correlated between the neutrino and anti-neutrino running.

Figures 31 and 32 show the fractional systematic uncertainties for the appearance and disappearance reconstructed energy spectra in neutrino mode and anti-neutrino mode, respectively. Black lines represent the prior uncertainties and bin widths of the systematic parameters f_i , while colored lines show the contribution from each uncertainty source. Figure 33 shows the correlation matrix of the systematic uncertainties between the reconstructed neutrino energy bins of the four samples. The systematic uncertainties (in %) of the number of expected events at the far detector are summarized in Table XXI.

D. Expected sensitivity to CP violation

Figure 34 shows the 90% CL allowed regions on the $\sin^2 2\theta_{13}$ - δ_{CP} plane. The results for the true values of $\delta_{CP} = (-90^\circ, 0, 90^\circ, 180^\circ)$ are overlaid. The top (bottom) plot shows the case for the normal (inverted) mass hierarchy. The value of δ_{CP} will be determined well. Also shown are

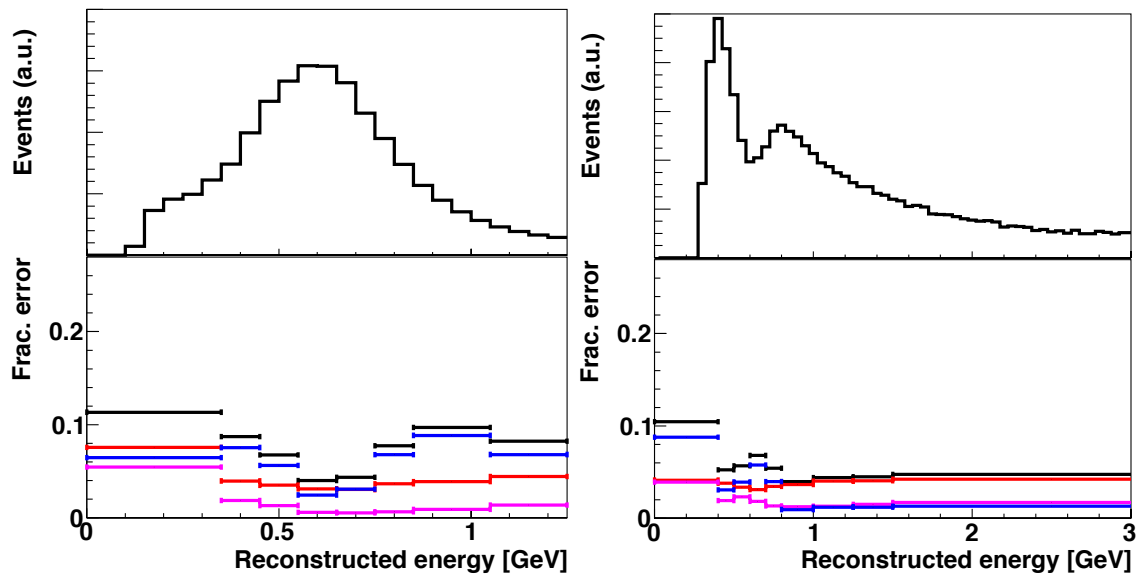


FIG. 31. Fractional error size for the appearance (left) and the disappearance (right) reconstructed energy spectra (bottom plots) in the neutrino mode. Black: total uncertainty, red: the flux and cross-section constrained by the near detector, magenta: the near detector non-constrained cross section, blue: the far detector error.

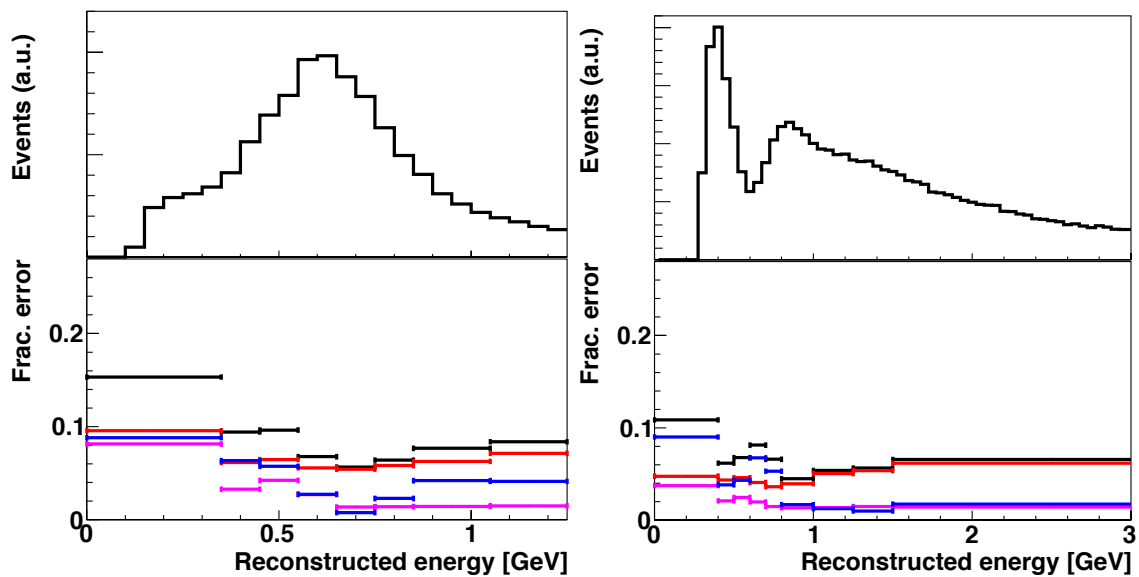


FIG. 32. Fractional error size for the appearance (left) and the disappearance (right) reconstructed energy spectra (bottom plots) in the anti-neutrino mode. Black: total uncertainty, red: the flux and cross-section constrained by the near detector, magenta: the near detector non-constrained cross section, blue: the far detector error.

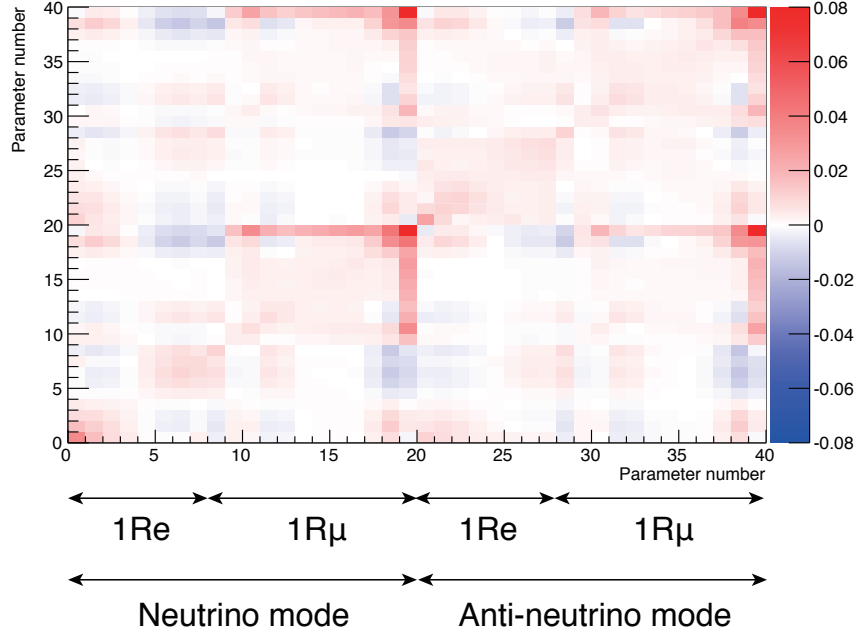


FIG. 33. Correlation matrix between reconstructed energy bins of the four samples due to the systematic uncertainties. Bins 1–8, 9–20, 21–28, and 29–40 correspond to the neutrino mode single ring e -like, the neutrino mode single ring μ -like, the anti-neutrino mode single ring e -like, and the anti-neutrino mode single ring μ -like samples, respectively.

TABLE XXI. Uncertainties (in %) for the expected number of events at Hyper-K from the systematic uncertainties assumed in this study.

Source	ν mode		$\bar{\nu}$ mode	
	Appearance	Disappearance	Appearance	Disappearance
Flux & ND-constrained cross section	3.0	2.8	5.6	4.2
ND-independent cross section	1.2	1.5	2.0	1.4
Far detector	0.7	1.0	1.7	1.1
Total	3.3	3.3	6.2	4.5

the allowed regions when we include a constraint on $\sin^2 2\theta_{13}$ from the reactor experiments. The $\sin^2 2\theta_{13}$ uncertainty of 0.005 is assumed. With reactor constraints, although the contour becomes narrower in the direction of $\sin^2 2\theta_{13}$, the sensitivity to δ_{CP} does not significantly change.

Figure 35 shows the expected significance to exclude $\sin \delta_{CP} = 0$ (the CP conserved case). The significance is calculated as $\sqrt{\Delta\chi^2}$, where $\Delta\chi^2$ is the difference of χ^2 for the *trial* value of δ_{CP} and for $\delta_{CP} = 0^\circ$ or 180° (the smaller value of difference is taken). We have also studied the case

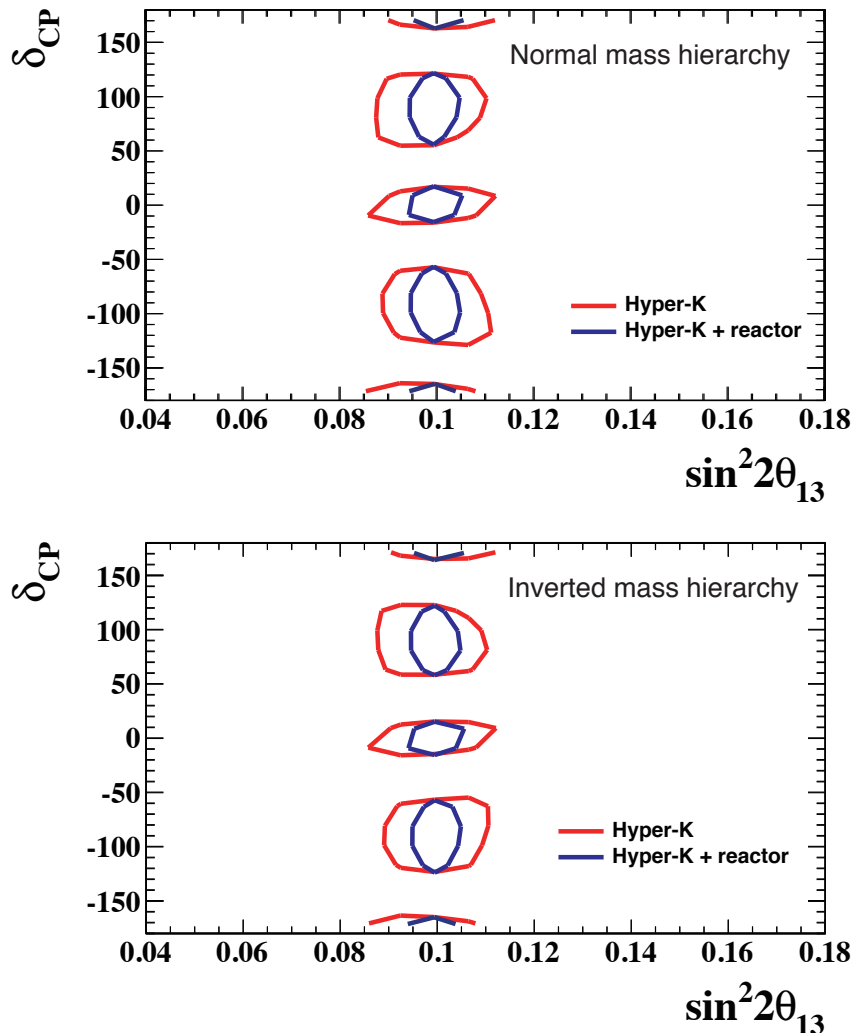


FIG. 34. The 90% CL allowed regions in the $\sin^2 2\theta_{13}$ - δ_{CP} plane. The results for the true values of $\delta_{CP} = (-90^\circ, 0, 90^\circ, 180^\circ)$ are overlaid. Top: normal hierarchy case. Bottom: inverted hierarchy case. Red (blue) lines show the result with Hyper-K only (with $\sin^2 2\theta_{13}$ constraint from reactor experiments).

with a reactor constraint but the result changes only slightly. Figure 36 shows the fraction of δ_{CP} for which $\sin \delta_{CP} = 0$ is excluded with more than 3σ and 5σ of significance as a function of the integrated beam power. The ratio of integrated beam power for the neutrino and anti-neutrino mode is fixed to 1:3. The normal mass hierarchy is assumed. The results for the inverted hierarchy is almost the same. CP violation in the lepton sector can be observed with more than $3(5)\sigma$ significance for 76(58)% of the possible values of δ_{CP} .

Figure 37 shows the 1σ uncertainty of δ_{CP} as a function of the integrated beam power. With $7.5 \text{ MW} \times 10^7 \text{ sec}$ of exposure (1.56×10^{22} protons on target), the value of δ_{CP} can be determined to better than 19° for all values of δ_{CP} .

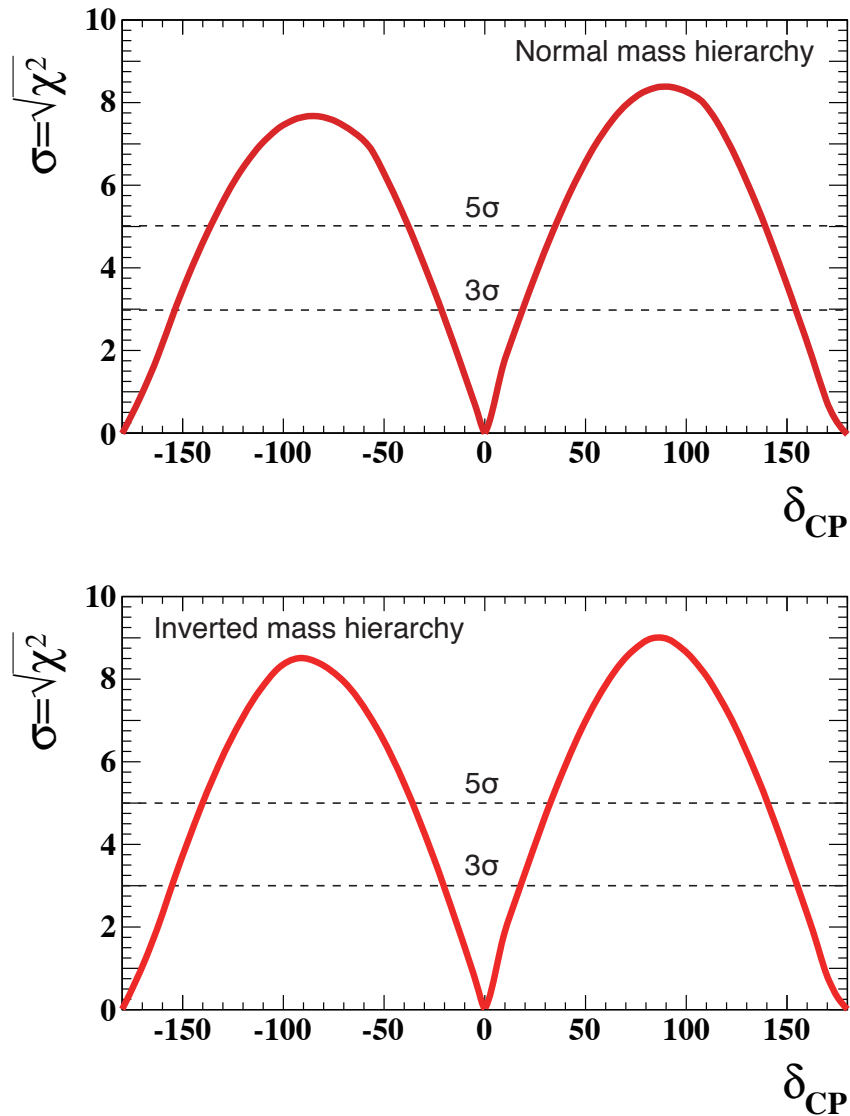


FIG. 35. Expected significance to exclude $\sin \delta_{CP} = 0$. Top: normal hierarchy case. Bottom: inverted hierarchy case.

E. Sensitivity to Δm_{32}^2 and $\sin^2 \theta_{23}$

The result shown above is obtained with $\sin^2 \theta_{23}$ and Δm_{32}^2 as free parameters as well as $\sin^2 2\theta_{13}$ and δ_{CP} , with a nominal parameters shown in Table XVIII. The use of ν_μ sample in addition to ν_e enables us to also measure $\sin^2 \theta_{23}$ and Δm_{32}^2 . Figure 38 shows the 90% CL allowed regions for the true value of $\sin^2 \theta_{23} = 0.5$. Hyper-K will be able to provide a precise measurement of $\sin^2 \theta_{23}$ and Δm_{32}^2 . Figure 39 shows the 90% CL allowed regions on the $\sin^2 \theta_{23}$ - Δm_{32}^2 plane, for the true values of $\sin^2 \theta_{23} = 0.45$ and $\Delta m_{32}^2 = 2.4 \times 10^{-3} \text{ eV}^2$. With a constraint on $\sin^2 2\theta_{13}$ from the

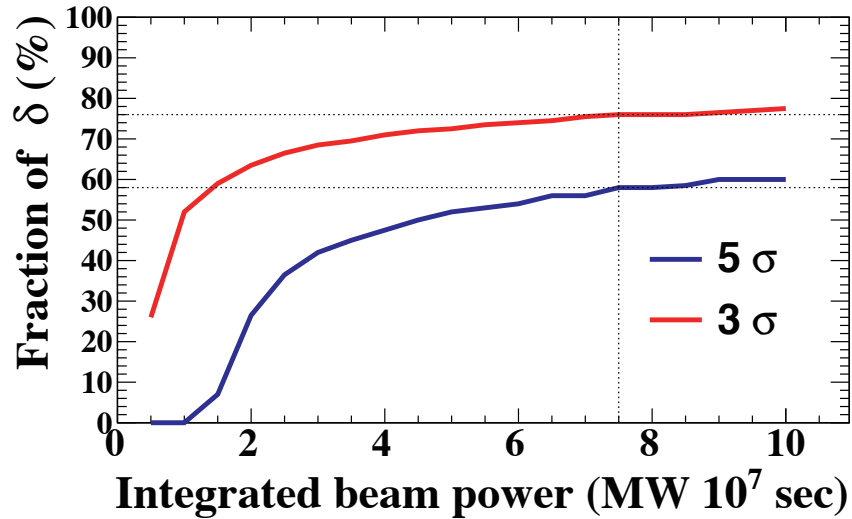


FIG. 36. Fraction of δ_{CP} for which $\sin \delta_{CP} = 0$ can be excluded with 3σ (red) and 5σ (blue) significance as a function of the integrated beam power. For the normal hierarchy case. The ratio of neutrino and anti-neutrino mode is fixed to 1:3.

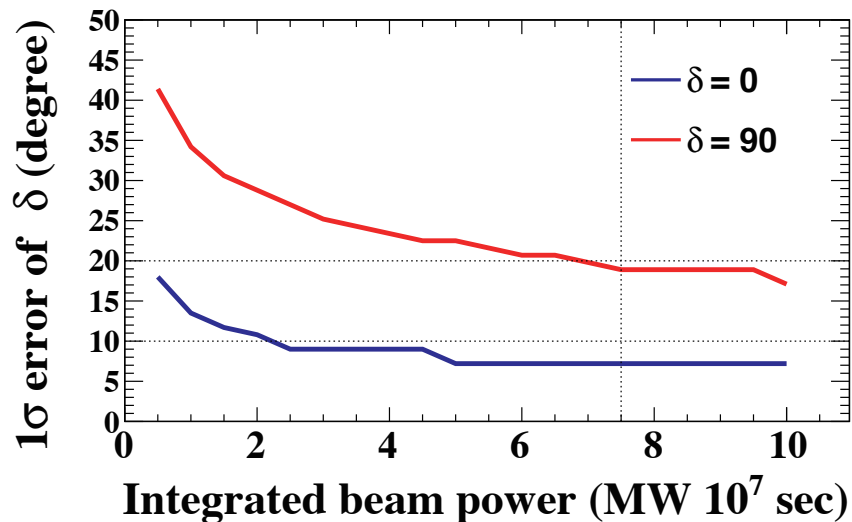


FIG. 37. Expected 1σ uncertainty of δ_{CP} as a function of integrated beam power.

reactor experiments, the octant degeneracy is resolved and θ_{23} can be precisely measured.

The expected precision of Δm_{23}^2 and $\sin^2 \theta_{23}$ for true $\sin^2 \theta_{23} = 0.45, 0.50, 0.55$ with reactor constraint on $\sin^2 2\theta_{13}$ is summarized in Table XXII.

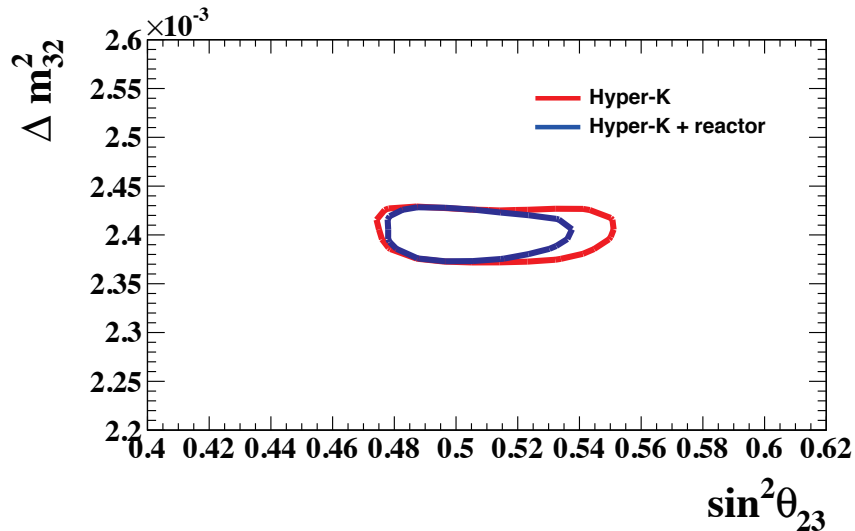


FIG. 38. The 90% CL allowed regions in the $\sin^2 \theta_{23} - \Delta m_{32}^2$ plane. The true values are $\sin^2 \theta_{23} = 0.5$ and $\Delta m_{32}^2 = 2.4 \times 10^{-3} \text{ eV}^2$. Effect of systematic uncertainties is included. The red (blue) line corresponds to the result with Hyper-K alone (with reactor constraints on $\sin^2 2\theta_{13}$).

TABLE XXII. Expected 1σ uncertainty of Δm_{23}^2 and $\sin^2 \theta_{23}$ for true $\sin^2 \theta_{23} = 0.45, 0.50, 0.55$. Reactor constraint on $\sin^2 2\theta_{13} = 0.1 \pm 0.005$ is imposed.

True $\sin^2 \theta_{23}$	0.45		0.50		0.55	
Parameter	Δm_{32}^2	$\sin^2 \theta_{23}$	Δm_{23}^2	$\sin^2 \theta_{23}$	Δm_{32}^2	$\sin^2 \theta_{23}$
Normal hierarchy	$1.4 \times 10^{-5} \text{ eV}^2$	0.006	$1.4 \times 10^{-5} \text{ eV}^2$	0.015	$1.5 \times 10^{-5} \text{ eV}^2$	0.009
Inverted hierarchy	$1.5 \times 10^{-5} \text{ eV}^2$	0.006	$1.4 \times 10^{-5} \text{ eV}^2$	0.015	$1.5 \times 10^{-5} \text{ eV}^2$	0.009

F. Combination with atmospheric neutrino data

Atmospheric neutrinos can provide an independent and complementary information to the accelerator beam program on the study of neutrino oscillation. For example, through the matter effect inside the Earth, a large statistics sample of atmospheric neutrinos by Hyper-K will have a good sensitivity to the mass hierarchy and θ_{23} octant.

Assuming a 10 year exposure, Hyper-K's sensitivity to the mass hierarchy and the octant of θ_{23} by atmospheric neutrino data are shown in Fig. 40. Depending upon the true value of θ_{23} the sensitivity changes considerably, but for all currently allowed values of this parameter the mass hierarchy sensitivity exceeds 3σ independent of the assumed hierarchy. If θ_{23} is non-maximal, the

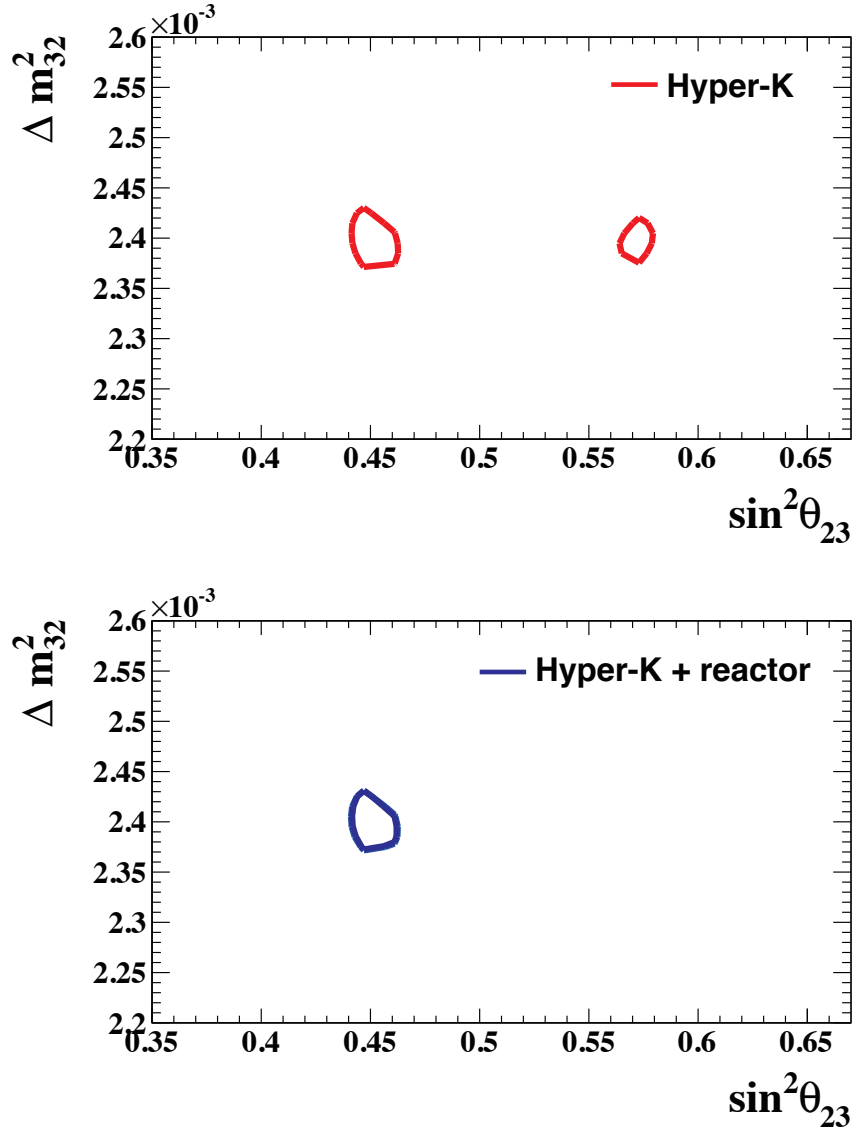


FIG. 39. 90% CL allowed regions in the $\sin^2 \theta_{23}$ - Δm_{32}^2 plane. The true values are $\sin^2 \theta_{23} = 0.45$ and $\Delta m_{32}^2 = 2.4 \times 10^{-3} \text{ eV}^2$. Effect of systematic uncertainties is included. Top: Hyper-K only. Bottom: With reactor constraint.

atmospheric neutrino data can be used to discriminate the octant at 3σ if $\sin^2 2\theta_{23} < 0.99$.

In the previous sections, the mass hierarchy is assumed to be known prior to the Hyper-K measurements. This is a reasonable assumption considering the increased opportunities, thanks to a large value of θ_{13} , of ongoing and proposed projects for mass hierarchy determination. However, even if the mass hierarchy is unknown before the start of experiment, Hyper-K itself will be able to determine it with the atmospheric neutrino measurements.

Because Hyper-K will observe both accelerator and atmospheric neutrinos with the same de-

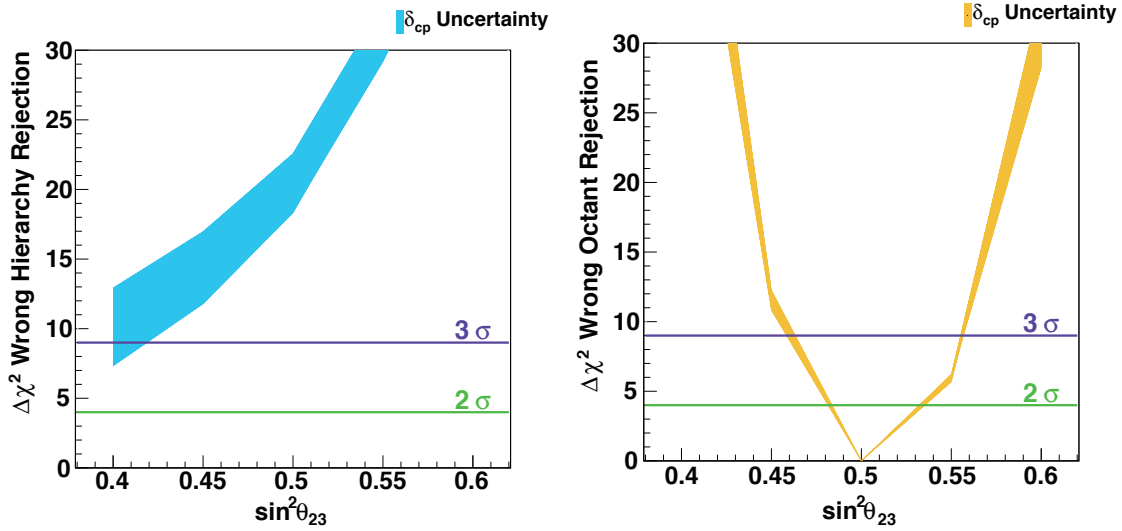


FIG. 40. Atmospheric neutrino sensitivities for a ten year exposure of Hyper-K assuming the mass hierarchy is normal. Left: the $\Delta \chi^2$ discrimination of the wrong hierarchy hypothesis as a function of the assumed true value of $\sin^2 \theta_{23}$. Right: the discrimination between the wrong octant for each value of $\sin^2 \theta_{23}$. The uncertainty from δ_{CP} is represented by the thickness of the band.

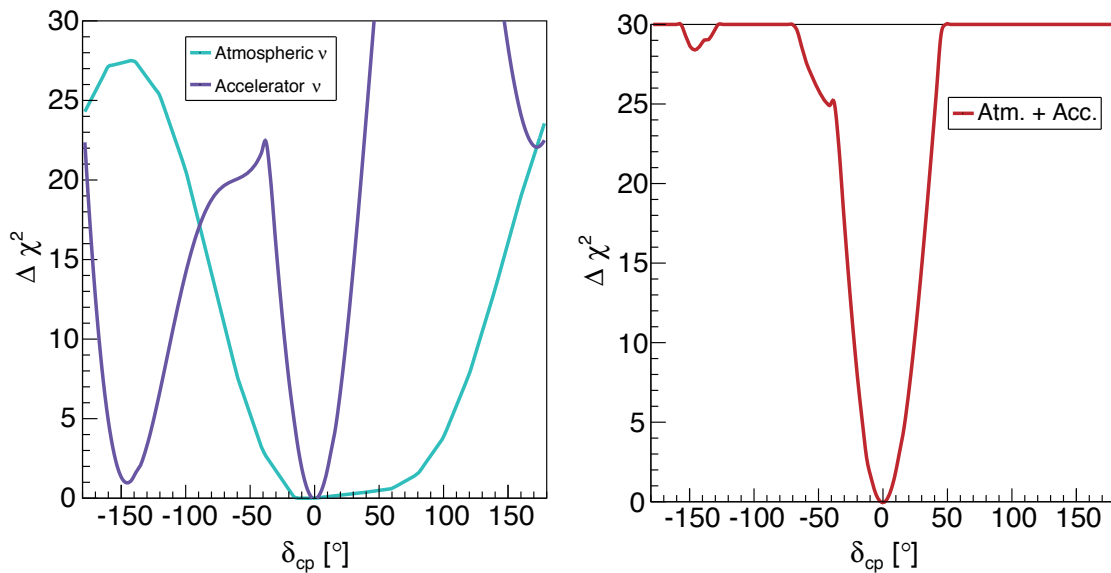


FIG. 41. Combination of the accelerator and atmospheric data. Left: Expected $\Delta \chi^2$ values for accelerator and atmospheric neutrino measurements assuming that the mass hierarchy is unknown. The true mass hierarchy is normal hierarchy and the true value of $\delta_{CP} = 0$. Right: By combining the two measurements, the sensitivity can be enhanced. In this example study, the $\Delta \chi^2$ is simply added.

tector, the physics capability of the project can be enhanced by combining two complementary measurements. As a demonstration of such a capability, a study is done by simply adding $\Delta\chi^2$ from two measurements, although in a real experiment more sophisticated analysis is expected. Assuming the true mass hierarchy of normal hierarchy and the true value of $\delta_{CP} = 0$, the values of expected $\Delta\chi^2$ as a function of δ_{CP} for each of accelerator and atmospheric neutrino measurements, *without* assumption of the prior mass hierarchy knowledge, are shown in the left plot of Fig. 41. For the accelerator neutrino measurement, there is a second minimum near $\delta_{CP} = 150^\circ$ because of a degeneracy with mass hierarchy assumptions. On the other hand, the atmospheric neutrino measurement can discriminate the mass hierarchy but the sensitivity to the CP violating phase δ_{CP} is worse than the accelerator measurement. By adding the information from both measurements, as shown in the right plot of Fig. 41, the fake solution can be eliminated and a precise measurement of δ_{CP} will be possible.

G. Summary

The sensitivity to leptonic CP asymmetry of a long baseline experiment using a neutrino beam directed from J-PARC to the Hyper-Kamiokande detector has been studied based on a full simulation of beamline and detector. With an integrated beam power of $7.5 \text{ MW} \times 10^7 \text{ sec}$, the value of δ_{CP} can be determined to better than 19° for all values of δ_{CP} and CP violation in the lepton sector can be observed with more than 3σ (5σ) significance for 76% (58%) of the possible values of δ_{CP} .

-
- [1] K. Abe, T. Abe, H. Aihara, Y. Fukuda, Y. Hayato, *et al.*, (2011), Letter of Intent: The Hyper-Kamiokande Experiment — Detector Design and Physics Potential —, arXiv:1109.3262 [hep-ex].
 - [2] J. Beringer *et al.* (Particle Data Group), Phys. Rev. **D86**, 010001 (2012).
 - [3] Y. Fukuda *et al.* (Super-Kamiokande), Phys. Rev. Lett. **81**, 1562 (1998), arXiv:hep-ex/9807003.
 - [4] P. Minkowski, Phys. Lett. **B67**, 421 (1977).
 - [5] M. Gell-Mann, P. Ramond, and R. Slansky, Conf. Proc. **C790927**, 315 (1979), arXiv:1306.4669 [hep-th].
 - [6] T. Yanagida, Conf. Proc. **C7902131**, 95 (1979).
 - [7] R. N. Mohapatra and G. Senjanovic, Phys. Rev. Lett. **44**, 912 (1980).
 - [8] M. Fukugita and T. Yanagida, Phys. Lett. **B174**, 45 (1986).

- [9] S. Fukuda *et al.* (Super-Kamiokande Collaboration), Phys. Rev. Lett. **86**, 5656 (2001), arXiv:hep-ex/0103033 [hep-ex].
- [10] K. Abe *et al.* (T2K Collaboration), Phys. Rev. Lett. **107**, 041801 (2011), arXiv:1106.2822 [hep-ex].
- [11] K. Abe *et al.* (T2K Collaboration), Phys. Rev. Lett. **112**, 061802 (2014), arXiv:1311.4750 [hep-ex].
- [12] J. C. Pati and A. Salam, Phys. Rev. Lett. **31**, 661 (1973).
- [13] H. Georgi and S. L. Glashow, Phys. Rev. Lett. **32**, 438 (1974).
- [14] P. Langacker, Phys. Rept. **72**, 185 (1981).
- [15] Z. Maki, M. Nakagawa, and S. Sakata, Prog. Theor. Phys. **28**, 870 (1962).
- [16] N. Cabibbo, Phys. Rev. Lett. **10**, 531 (1963).
- [17] M. Kobayashi and T. Maskawa, Prog. Theor. Phys. **49**, 652 (1973).
- [18] B. Pontecorvo, Sov. Phys. JETP **26**, 984 (1968).
- [19] J. Schechter and J. Valle, Phys. Rev. **D22**, 2227 (1980).
- [20] S. M. Bilenky, J. Hosek, and S. Petcov, Phys. Lett. **B94**, 495 (1980).
- [21] M. Doi, T. Kotani, H. Nishiura, K. Okuda, and E. Takasugi, Phys. Lett. **B102**, 323 (1981).
- [22] Q. Ahmad *et al.* (SNO Collaboration), Phys. Rev. Lett. **89**, 011301 (2002), arXiv:nucl-ex/0204008 [nucl-ex].
- [23] Q. Ahmad *et al.* (SNO Collaboration), Phys. Rev. Lett. **87**, 071301 (2001), arXiv:nucl-ex/0106015 [nucl-ex].
- [24] K. Abe *et al.* (Super-Kamiokande Collaboration), Phys. Rev. **D83**, 052010 (2011), arXiv:1010.0118 [hep-ex].
- [25] K. Eguchi *et al.* (KamLAND Collaboration), Phys. Rev. Lett. **90**, 021802 (2003), arXiv:hep-ex/0212021 [hep-ex].
- [26] T. Araki *et al.* (KamLAND Collaboration), Phys. Rev. Lett. **94**, 081801 (2005), arXiv:hep-ex/0406035 [hep-ex].
- [27] S. Abe *et al.* (KamLAND Collaboration), Phys. Rev. Lett. **100**, 221803 (2008), arXiv:0801.4589 [hep-ex].
- [28] Y. Ashie *et al.* (Super-Kamiokande Collaboration), Phys. Rev. **D71**, 112005 (2005), arXiv:hep-ex/0501064 [hep-ex].
- [29] Y. Ashie *et al.* (Super-Kamiokande Collaboration), Phys. Rev. Lett. **93**, 101801 (2004), arXiv:hep-ex/0404034 [hep-ex].
- [30] M. Ahn *et al.* (K2K Collaboration), Phys. Rev. **D74**, 072003 (2006), arXiv:hep-ex/0606032 [hep-ex].
- [31] P. Adamson *et al.* (MINOS Collaboration), Phys. Rev. Lett. **106**, 181801 (2011), arXiv:1103.0340 [hep-ex].
- [32] P. Adamson *et al.* (MINOS Collaboration), Phys. Rev. Lett. **107**, 181802 (2011), arXiv:1108.0015 [hep-ex].
- [33] Y. Abe *et al.* (DOUBLE-CHOOZ Collaboration), Phys. Rev. Lett. **108**, 131801 (2012), arXiv:1112.6353 [hep-ex].

- [34] J. Ahn *et al.* (RENO collaboration), Phys. Rev. Lett. **108**, 191802 (2012), arXiv:1204.0626 [hep-ex].
- [35] F. An *et al.* (DAYA-BAY Collaboration), Phys. Rev. Lett. **108**, 171803 (2012), arXiv:1203.1669 [hep-ex].
- [36] J. Arafune, M. Koike, and J. Sato, Phys. Rev. **D56**, 3093 (1997), arXiv:hep-ph/9703351 [hep-ph].
- [37] V. D. Barger, K. Whisnant, and R. Phillips, Phys. Rev. Lett. **45**, 2084 (1980).
- [38] S. Pakvasa, AIP Conf. Proc. **68**, 1164 (1980).
- [39] C. Jarlskog, Phys. Rev. Lett. **55**, 1039 (1985).
- [40] “Physics Potential and Sensitivities of T2K,” T2K Report to 17th J-PARC PAC, Sep. 2013. <http://www.t2k.org/docs/pub/015>.
- [41] F. Capozzi, G. Fogli, E. Lisi, A. Marrone, D. Montanino, *et al.*, (2013), arXiv:1312.2878 [hep-ph].
- [42] H. Nishino, K. Awai, Y. Hayato, S. Nakayama, K. Okumura, *et al.*, Nucl. Instrum. Meth. **A610**, 710 (2009), arXiv:0911.0986 [physics.ins-det].
- [43] AMT-2 & 3 (ATLAS Muon TDC version 2 & 3) Data Sheets, <http://atlas.kek.jp/tdc/amt3/index.html>.
- [44] K. Abe, Y. Hayato, T. Iida, K. Iyogi, J. Kameda, *et al.*, Nucl. Instrum. Meth. **A737**, 253 (2014), arXiv:1307.0162 [physics.ins-det].
- [45] Subversion repository for WCSim: <http://svn.phy.duke.edu/repos/neutrino/dusel/WCSim/>.
- [46] S. Agostinelli *et al.* (GEANT4), Nucl. Instrum. Meth. **A506**, 250 (2003).
- [47] J. Allison, K. Amako, J. Apostolakis, H. Araujo, P. Dubois, *et al.*, IEEE Trans. Nucl. Sci. **53**, 270 (2006).
- [48] R. Brun, F. Carminati, and S. Giani, (1994), , CERN-W5013.
- [49] “J-PARC TDR,” (2003), KEK Report 2002-13 and JAERI-Tech 2003-44.
- [50] K. Abe *et al.* (T2K Collaboration), Nucl. Instrum. Meth. **A659**, 106 (2011).
- [51] D. Beavis, A. Carroll, I. Chiang, *et al.*, (1995), Long Baseline Neutrino Oscillation Experiment at the AGS(Proposal E889), Physics Design Report, BNL-52459.
- [52] S. Bhadra *et al.*, Nucl. Instrum. Meth. **A703**, 45 (2013).
- [53] S. Igarashi, “Towards 0.75 MW MR FX, MR upgrade plan,” Talk presented at J-PARC Accelerator Technical Advisory Committee (ATAC-2014), Tokai, Japan, Mar. 2014.
- [54] Y. Sato (J-PARC Main Ring commissioning group), “Toward J-PARC MR FX 750 kW,” Talk presented at the 1st workshop on next generation accelerator-based neutrino experiment, Tokai, Japan, Feb. 2014.
- [55] S. Igarashi, H. Harada, H. Hotchi, T. Koseki, and Y. Sato, “Accelerator Concepts for Multi-MW,” Talk presented at the 1st workshop on next generation accelerator-based neutrino experiment, Tokai, Japan, Feb. 2014.
- [56] Y. Yamada (J-PARC neutrino beamline group), “J-PARC Neutrino beamline, present limits on beam power,” Talk presented at the 1st workshop on next generation accelerator-based neutrino experiment, Tokai, Japan, Feb. 2014.
- [57] M. Tada (J-PARC neutrino beamline group), “Neutrino beamline for multiple MW beam,” Talk presented at the 1st workshop on next generation accelerator-based neutrino experiment, Tokai, Japan,

Feb. 2014.

- [58] K. Abe *et al.* (T2K Collaboration), Phys. Rev. **D87**, 012001 (2013), arXiv:1211.0469 [hep-ex].
- [59] N. Abgrall *et al.* (NA61/SHINE Collaboration), Phys. Rev. **C84**, 034604 (2011), arXiv:1102.0983 [hep-ex].
- [60] N. Abgrall *et al.* (NA61/SHINE Collaboration), Phys. Rev. **C85**, 035210 (2012), arXiv:1112.0150 [hep-ex].
- [61] N. Abgrall *et al.* (NA61/SHINE Collaboration), Nucl. Instrum. Meth. **A701**, 99 (2013), arXiv:1207.2114 [hep-ex].
- [62] M. Day and K. S. McFarland, Phys. Rev. **D86**, 053003 (2012), arXiv:1206.6745 [hep-ph].
- [63] J. Marteau, Eur. Phys. J. **A5**, 183 (1999), arXiv:hep-ph/9902210 [hep-ph].
- [64] M. Martini, M. Ericson, G. Chanfray, and J. Marteau, Phys. Rev. **C80**, 065501 (2009), arXiv:0910.2622 [nucl-th].
- [65] J. Carlson, J. Jourdan, R. Schiavilla, and I. Sick, Phys. Rev. **C65**, 024002 (2002), arXiv:nucl-th/0106047 [nucl-th].
- [66] G. Shen, L. Marcucci, J. Carlson, S. Gandolfi, and R. Schiavilla, Phys. Rev. **C86**, 035503 (2012), arXiv:1205.4337 [nucl-th].
- [67] A. Bodek, H. Budd, and M. Christy, Eur. Phys. J. **C71**, 1726 (2011), arXiv:1106.0340 [hep-ph].
- [68] M. Martini, M. Ericson, G. Chanfray, and J. Marteau, Phys. Rev. **C81**, 045502 (2010), arXiv:1002.4538 [hep-ph].
- [69] M. Martini and M. Ericson, Phys. Rev. **C87**, 065501 (2013), arXiv:1303.7199 [nucl-th].
- [70] J. Nieves, M. Valverde, and M. Vicente Vacas, Phys. Rev. **C73**, 025504 (2006), arXiv:hep-ph/0511204 [hep-ph].
- [71] J. Nieves, I. R. Simo, and M. J. V. Vacas, Phys. Rev. C **83**, 045501 (2011).
- [72] A. Aguilar-Arevalo *et al.* (MiniBooNE Collaboration), Phys. Rev. **D81**, 092005 (2010), arXiv:1002.2680 [hep-ex].
- [73] A. Aguilar-Arevalo *et al.* (MiniBooNE Collaboration), Phys. Rev. **D88**, 032001 (2013), arXiv:1301.7067 [hep-ex].
- [74] L. Fields *et al.* (MINERvA Collaboration), Phys. Rev. Lett. **111**, 022501 (2013), arXiv:1305.2234 [hep-ex].
- [75] G. Fiorentini *et al.* (MINERvA Collaboration), Phys. Rev. Lett. **111**, 022502 (2013), arXiv:1305.2243 [hep-ex].
- [76] M. Otani, N. Nagai, D. Orme, A. Minamino, K. Nitta, *et al.*, Nucl. Instrum. Meth. **A623**, 368 (2010).
- [77] S. Assylbekov *et al.*, Nucl. Instrum. Meth. **A686**, 48 (2012).
- [78] N. Abgrall *et al.* (T2K ND280 TPC Collaboration), Nucl. Instrum. Meth. **A637**, 25 (2011).
- [79] P. Amaudruz *et al.* (T2K ND280 FGD Collaboration), Nucl. Instrum. Meth. **A696**, 1 (2012).
- [80] S. Aoki, G. Barr, M. Batkiewicz, J. Blocki, J. Brinson, *et al.*, Nucl. Instrum. Meth. **A698**, 135 (2013), arXiv:1206.3553 [physics.ins-det].

- [81] K. Abe *et al.* (T2K Collaboration), (2014), arXiv:1403.1532 [hep-ex].
- [82] K. Abe *et al.* (T2K Collaboration), (2014), arXiv:1403.2552 [hep-ex].
- [83] K. Abe *et al.*, “A letter of intent to extend T2K with a detector 2 km away from the JPARC neutrino source,” http://j-parc.jp/researcher/Hadron/en/pac_0707/pdf/2km-loi-final-070628.pdf (2007).
- [84] A. Aguilar-Arevalo *et al.* (MiniBooNE Collaboration), Nucl. Instrum. Meth. **A599**, 28 (2009), arXiv:0806.4201 [hep-ex].
- [85] I. Anghel, J. Beacom, M. Bergevin, G. Davies, F. Di Lodovico, *et al.*, (2014), arXiv:1402.6411 [physics.ins-det].
- [86] M. Martini, M. Ericson, G. Chanfray, and J. Marteau, Phys. Rev. **C80**, 065501 (2009), arXiv:0910.2622 [nucl-th].
- [87] E. Piasezky, M. Sargsian, L. Frankfurt, M. Strikman, and J. Watson, Phys. Rev. Lett. **97**, 162504 (2006), arXiv:nucl-th/0604012 [nucl-th].
- [88] C. Adams *et al.* (LBNE Collaboration), (2013), arXiv:1307.7335 [hep-ex].
- [89] F. An *et al.* (Daya Bay Collaboration), Phys. Rev. Lett. **112**, 061801 (2014), arXiv:1310.6732 [hep-ex].
- [90] Y. Abe *et al.* (Double Chooz Collaboration), (2014), arXiv:1401.5981 [hep-ex].
- [91] Y. Hayato, Nucl. Phys. Proc. Suppl. **112**, 171 (2002).
- [92] G. Mitsuka, AIP Conf. Proc. **967**, 208 (2007).
- [93] G. Mitsuka, AIP Conf. Proc. **981**, 262 (2008).